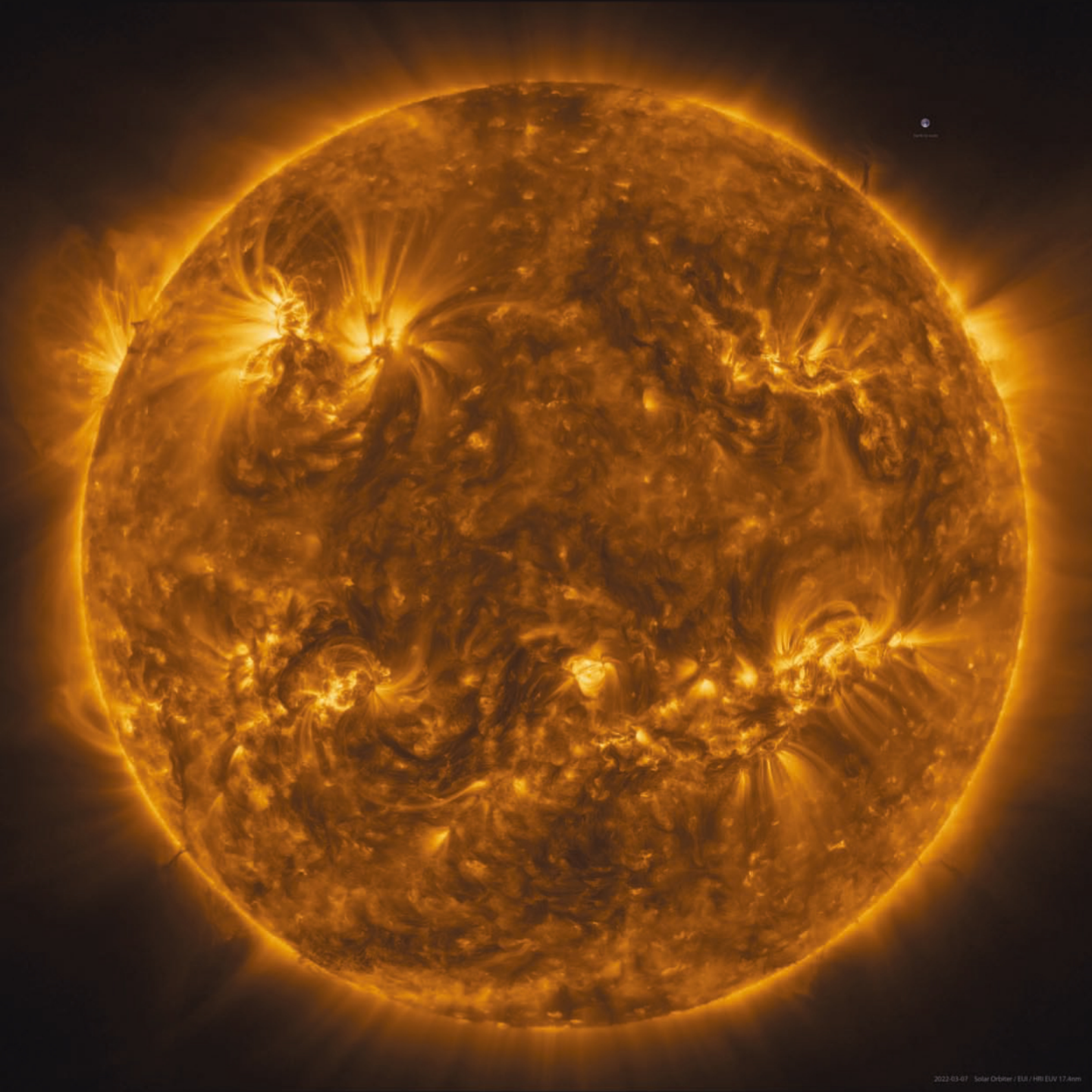


# HIPPARCHOS

The Hellenic Astronomical Society Newsletter

Volume 3, Issue 6

ISSN: 1790-9252





# Contents

**HIPPARCHOS**

Volume 3, Issue 6 • June 2023

ISSN: 1790-9252

Hipparchos is the official newsletter of the Hellenic Astronomical Society. It publishes review papers, news and comments on topics of interest to astronomers, including matters concerning members of the Hellenic Astronomical Society.

## Editorial board

- **Georgios Balasis**  
(National Observatory of Athens)
- **Konstantinos Gourgouliatos**  
(University of Patras)
- **Elias Koulouridis**  
(National Observatory of Athens)
- **Konstantinos Tassis**  
(University of Crete)

## Contact person

Georgios Balasis  
Institute for Astronomy, Astrophysics,  
Space Applications and Remote  
Sensing (IAASARS), National  
Observatory of Athens (NOA)  
Lofos Nymphon, PO Box 20048,  
11810, Athens  
Tel: +30-210 810 9185  
E-mail: gbalasis@noa.gr

## Editorial Advisors

- **Vassilis Charmandaris**  
(University of Crete)
- **Athanasios Papaioannou**  
(National Observatory of Athens)
- **Maria Petropoulou**  
(National and Kapodistrian  
University of Athens)

Printed by ZITI Publications • www.ziti.gr

**Message from the President** ..... 3

## REVIEWS

**Developments of the third integral**  
by George Contopoulos ..... 4

**Episodic Mass Loss in Evolved Massive Stars**  
by Alceste Z. Bonanos ..... 10

**Galaxy evolution; lessons, challenges, and opportunities  
in the golden era of observational astrophysics**  
by Georgios E. Magdis ..... 15

**Geomagnetically Induced Currents:  
a potential threat to our technological world**  
by Adamantia Zoe Boutsis and George Balasis ..... 20

**The 16th Hellenic Astronomical Conference**  
26 - 28 June 2023, Athens ..... 26



## Cover Image

The Sun as seen by Solar Orbiter in extreme ultraviolet light from a distance of roughly 75 million kilometres. The image is a mosaic of 25 individual images taken on 7 March by the high resolution telescope of the Extreme Ultraviolet Imager (EUI) instrument. Taken at a wavelength of 17 nanometers, in the extreme ultraviolet region of the electromagnetic spectrum, this image reveals the Sun's upper atmosphere, the corona, which has a temperature of around a million degrees Celsius. In total, the final image contains more than 83 million pixels in a 9148 x 9112 pixel grid, making it the highest resolution image of the Sun's full disc and outer atmosphere, the corona, ever taken.

Credit: ESA & NASA/Solar Orbiter/EUI team; Data processing: E. Kraaikamp (ROB)

# Message from the President



This issue of Hipparchos, the third I have the honor to introduce as the President of our Society, follows a, by now, well-established tradition of presenting a number of high-quality reviews across the whole spectrum of areas of astrophysics and space physics: from galaxy evolution and the distant universe and, to the neighborhood of our home planet and the complex interactions with its magnetic field with the solar wind.

I would like to thank all authors for taking the time to prepare their articles at a level which is easily accessible even for the non-experts, while maintaining a scientific rigor.

In particular though would like to thank Dr. George Balasis, the Vice President of our Society who made this issue of Hipparchos, as well as a special issue which will also appear on the occasion of the 30<sup>th</sup> anniversary of the Society a real-

ity. Thanks to his hard work and attention to detail the Society has produced this year two more newsletters which are comparable or better to publications of Societies with much longer tradition, size, and resources than ours. I am certain that all of us will enjoy reading them.

This issue will be distributed during the 16<sup>th</sup> Conference of HelAS, which takes place in Athens between June 25 and 28, 2023. During the Conference we will also celebrate this major anniversary of HelAS and contemplate on its historic role in shaping Greek Astronomy. Even though I was only a graduate student when the Society was founded, I was fortunate to be a friend and remain in close contact with Prof. John Seiradakis, who played a key role in the establishment of the Society: first in the preparatory phases and then formally first as Secretary and then as President of HelAS. Unfortunately, John is no longer

with us, but when it comes to issues related to the Society and its role regarding the advancement of astronomy in Greece, I am certain that his gentle spirit lives in our memories and influences our decisions.

I believe that one aspect advocated by John was the importance of establishing close relations and interactions with colleagues, both professionally and socially. Learning about the scientific expertise of our colleagues and developing close personal relations with them, help us address all challenges more efficiently, as well as solve complex administrative problems, which require the coordinated effort of many.

This simple issue of Hipparchos, as well as our 16<sup>th</sup> Conference this June in Athens, bring us together and will hopefully contribute to make one more step forward in improving astronomy research and education in Greece.

---

*Vassilis Charmandaris*  
*President of Hel.A.S.*

---



# 1993-2023

# Developments of the third integral

by George Contopoulos

Research Center for Astronomy and Applied Mathematics of the Academy of Athens  
Soranou Efessiou 4, GR-11527 Athens, Greece • e-mail: gcontop@academyofathens.gr

## Abstract

We summarize the historical developments of the third integral. We emphasize the main new results, especially those concerning the convergent form of the third integral and its applications. Then we consider briefly the developments concerning the integrals in Relativity, Cosmology and Quantum Mechanics.

## 1. A short history of the third integral

It is well known that an axisymmetric conservative galactic potential has two integrals of motion, the energy and the angular momentum along the symmetry axis. In general there is no further integral although there is an infinity of integrable systems with 3 integrals (Lynden Bell 1962). However in many nonintegrable cases some people have found a formal third integral (Whittaker 1916, 1937, Cherry 1924ab, 1928, Contopoulos 1960 etc). This integral is found around an equilibrium point or a stable periodic orbit, in the form of a series. Although this series is not convergent it can give approximately the real orbits if it is truncated at a sufficiently high order (Nekhoroshev 1977, Contopoulos et al. 2003, Efthymiopoulos et al. 2004). Whittaker (1916, 1937) formulated an integral in action-angle variables and he called it "adelphic integral" because it has some similarities with the energy integral. Then Cherry (1924ab) introduced complex variables. We (Contopoulos 1960) used cartesian coordinates and applied the third integral in many dynamical problems, with emphasis on the dynamics of galaxies. In general the orbits on a meridian plane of an axisymmetric galaxy have the form of distorted Lissajous figures and are called "box orbits" (Fig. 1a, b). However, of particular interest are the resonant forms of the third integral (Contopou-

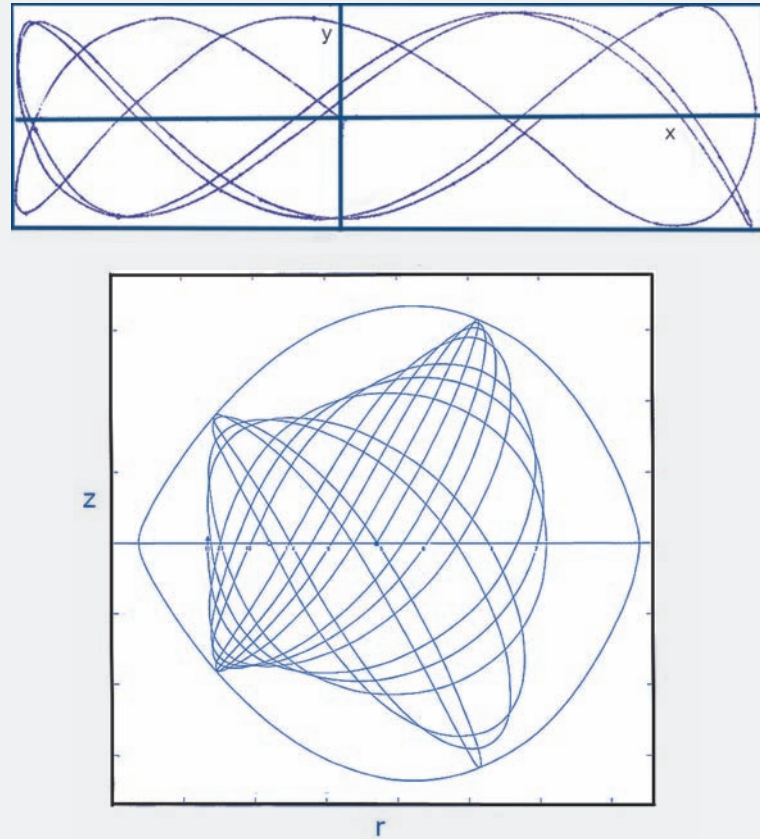


Figure 1: Box orbits in the meridian plane of a galaxy, (a) One of the very first calculated orbits (Contopoulos 1958) (b) an orbit calculated by Ollongren (1962).

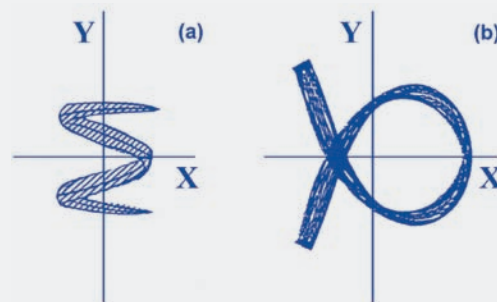


Figure 2: Resonant orbits close to stable periodic orbits, (a) near a 2/1 periodic orbit and (b) near a 2/3 periodic orbit.

los 1966ab) around particular resonant periodic orbits (Fig. 2a,b) in Hamiltonians, of the form

$$H = \frac{1}{2}(\dot{x}^2 + \dot{y}^2 + \omega_1^2 x^2 + \omega_2^2 y^2) + \epsilon(\text{hot})^1 \quad (1)$$

where  $\omega_1/\omega_2 = \text{rational}$ .

1. higher order terms in x and y.

As it was shown by Kolmogorov (1954), Arnold (1961) and Moser (1962), there is a set of invariant curves (KAM curves) around a stable equilibrium and around the intersections of stable periodic orbits by a Poincaré "surface of section". The special case  $\omega_1 = \omega_2$  provides orbits of the form of Fig. 3abc.

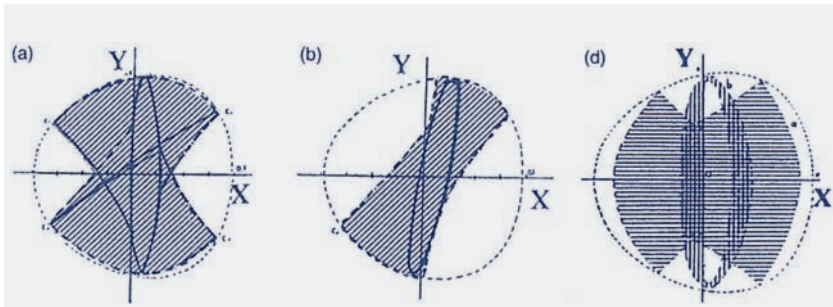


Figure 3: Types of orbits in the 1/1 resonance.

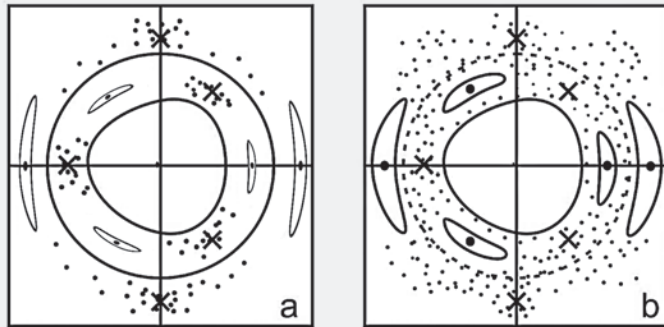


Figure 4: Resonance overlap (schematically). Solid curves represent invariant curves around the center and islands around stable periodic orbits (3 dots and 2 dots). Scattered points represent chaotic orbits around unstable periodic orbits (3X and 2X) (a) for a perturbation before the resonance overlap the 3/1 and 2/1 chaotic domains are separated (b) for a larger perturbation the 3/1 and 2/1 chaotic domains are joined.

The higher orders terms of the third integral were found by computer programs in Fortran (Contopoulos 1965, 1966b, Gustavson 1966). Then Giorgilli (1979) developed a most efficient program that gives integrals up to very high orders. Later Efthymiopoulos (2005) used programs that go to order 100 and higher. More recently we found the third integral in potentials periodic in time (Tzemos and Contopoulos 2020, 2021). If we stop the calculation at a small order we may find wrong results. E.g. Kaluza and Robnik (1992) calculated orbits in the Hénon-Heiles (1964) potential up to order 14 and all orbits appeared to be ordered. However, if we go beyond order 20 we find that most orbits are chaotic.

In general, the dynamical systems have both ordered and chaotic orbits. Ordered orbits appear near the stable periodic orbits. On the other hand, chaotic orbits appear mainly near unstable periodic orbits. But a large degree of chaos appears when we have ‘resonance overlap’. This phenomenon was described by Contopoulos (1966c) and by Rosenbluth et al. (1966). When the perturbation  $\epsilon$

is small the intersections of the orbits with a “surface of section” form islands around the stable periodic orbits. In Fig. 4a between the 3 and the 2 islands there are some chaotic orbits, mainly near the unstable periodic orbits. But the resonances 3 and 2 are well separated by a set of invariant curves around the origin. However as the perturbation increases the islands become larger and the separating invariant curves are destroyed. Thus, the chaotic domains are joined and a large degree of chaos appears. This mechanism was discussed in detail by Chirikov (1979)<sup>2</sup>.

The main criterion of chaos is provided by the Lyapunov characteristic number (LCN)

$$\text{LCN} = \lim_{t \rightarrow \infty} \chi \quad (2)$$

$$\text{where } \chi = \frac{\ln(\xi/\xi_0)}{t} \quad (3)$$

is the “finite time LCN” and  $\xi_0$  and  $\xi$  are

2. Thus, many people call this mechanism “Chirikov’s mechanism”. But Chirikov wrote on 23-10-68 to Contopoulos: “My criterion of stochasticity by resonance overlapping is essentially the same as yours in your paper in Bulletin Astronomique”, and he published his results in 1979.

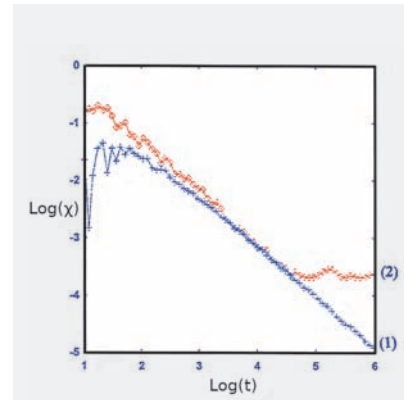


Figure 5: The “finite time LCN” of an ordered orbit (1) is  $\chi$  and tends to LCN = 0 as  $t \rightarrow \infty$  while it tends to a positive value of LCN  $\approx 10^{-4}$  for a chaotic orbit (2).

infinitesimal deviations from an orbit at times 0 and  $t$  (Fig.5). By calculating the LCN of a number of orbits we find the domains of order and chaos in a dynamical system.

As regards 3d systems, Contopoulos, Galgani and Giorgilli (1978) found cases in 3d systems with only one integral, two integrals and 3 integrals. One integral is the energy and the other integrals are formal of the form of the ‘third integral’.

The periodic orbits in 3d systems are divided into 4 categories (1) stable (2) simply unstable (3) doubly unstable and (4) complex unstable. All four types of periodic orbits appear in a general system. Around the stable orbits there is order and around the unstable orbits there is chaos.

Further developments and applications of the third integral can be found in the book (Contopoulos 2002).

## 2. Convergent third integrals (Moser series)

Near the unstable periodic orbits of non-integrable systems there is chaos. However, in this region the third integral converges. This is a strange fact that was noticed first by Cherry (1928) and in greater detail by Moser (1956, 1958). The proof of the convergence was completed by Giorgilli (2001). We call this form of the third integral “Moser series”. This is a most important discovery in recent years.

The reason for the convergence of the third integral near unstable points and its divergence near stable orbits is the following. The terms of the third integral have divisors of the form  $(m_1\omega_1 + m_2\omega_2)$

where  $m_1, m_2$  are positive or negative integers and  $\omega_1, \omega_2$  are the eigenvalues of the periodic orbit. These divisors may become very small, making the corresponding terms very large, and that fact does not allow convergence of the series<sup>3</sup>. However near an unstable orbit one eigenvalue is imaginary ( $\omega_2 = i\nu$ ) therefore the corresponding divisor does not ever become small, and convergence can be obtained. An application of the Moser series was made by da Silva Ritter et al. (1987), Vieira and de Almeida (1996) and de Almeida and Vieira (1997). In the case of the Hénon hyperbolic map

$$x' = \cosh(k)x + \sinh(k)(y - x^2/\sqrt{2}) \quad (4)$$

$$y' = \sinh(k)x + \cosh(k)(y - x^2/\sqrt{2}) \quad (5)$$

These authors introduced variables

$$u = (x + y)/\sqrt{2}, v = (x - y)/\sqrt{2} \quad (6)$$

and made a near identity transformation

$$u = \xi + \phi_{12} + \phi_{13} + \dots, v = \eta + \phi_{22} + \phi_{23} + \dots, \quad (7)$$

where the functions  $\phi_{ij}$  are such that the mapping is

$$\xi' = \Lambda\xi, \eta' = \eta/\Lambda \quad (8)$$

where  $\Lambda$  is a function of  $c = \xi\eta$ . Therefore in the variables  $\xi, \eta$  the mapping gives points on hyperbolae

$$\xi\eta' = \xi\eta = c \quad (9)$$

We have extended this work (Contopoulos and Harsoula 2015, Harsoula et al. 2016) and we present here our main conclusions.

The axes  $\xi = 0$  and  $\eta = 0$  ( $c = 0$ ) represent the stable and unstable asymptotic curves of the unstable periodic orbit  $(0, 0)$ . These two curves intersect each other at an infinity of homoclinic points. In Fig. 6a we have drawn the initial parts of these curves. While the asymptotic curves on the left extend to infinity, the curves on the right of the origin go to a maximum and then they make infinite oscillations close to the left curves.

In Fig. 6b we have drawn besides the asymptotic curves (red), two curves (blue) with  $c = 0.1$  in the regions 1 and 4

3. A study of the forms of the terms of the third integral leading to non-convergence was made by Contopoulos et al. (2003) and by Efthymiopoulos et al. (2004)

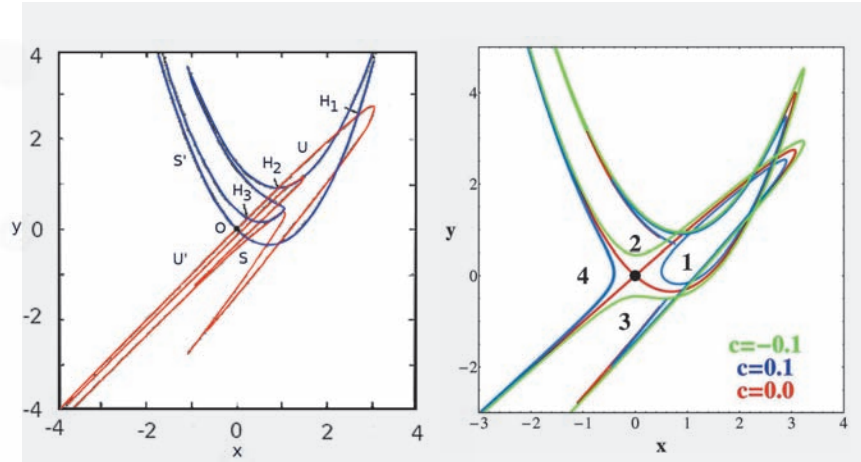


Figure 6: a) The asymptotic curves of the central unstable periodic orbit ( $S, S'$ =stable (blue),  $U, U'$ =unstable (red) for  $k = 1.43$ ) intersect at an infinity of homoclinic points, like  $H_1, H_2, H_3$  etc. b) Some invariant curves starting in the regions 1 and 4 (blue), 2 and 3 (green) together with the asymptotic curves (red).

and two more curves (green) in the regions 2 and 3 with  $c = -0.1$ . The corresponding curves in the variables  $\xi$  and  $\eta$  are given in Fig. 7. In this Figure we have drawn in red the limiting curves (red hyperbolae for  $c = c_{max} = 0.49$  (if  $k = 1.43$ ) where the series converge), and in blue the invariant curves  $c = \pm 0.1$ . The successive iterates of two points starting on the curve  $c = 0.1$  are given in Fig. 8a and they seem to be random. However, all these points lie on the curve  $c = 0.1$  and are given analytically by using the Moser series (Fig. 8b), truncated at a high order. Therefore, the positions of the successive iterates can be given analytically and they are not random.

The apparent randomness of the points of Fig. 9a is due to two facts: (1) the distance of successive iterates along the invariant curve increases as a power of the eigenvalue  $\lambda > 1$ , and (2) the curve  $c = const.$  makes several oscillations and comes an infinite number of times close to the origin, so that the distances of the successive points in  $x$  and  $y$  ( $\Delta x, \Delta y$ ) can be small and look random, although they can be calculated analytically.

Another feature of Fig. 8b is that in the region 1 there is an island of stability around a stable periodic orbit  $S$ . All the red points are outside the last KAM curve of this island. In fact, the invariant curve for  $c = 0.1$  does not intersect this island. However, for larger  $c$  the invariant curve intersects the last KAM curve and for even larger  $c$  (but smaller than  $c_{max}$ ) the whole Moser curve is inside the island. The limit-

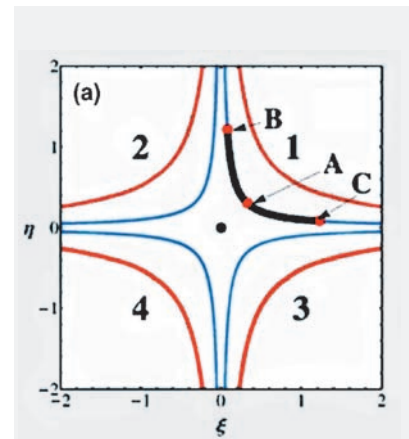
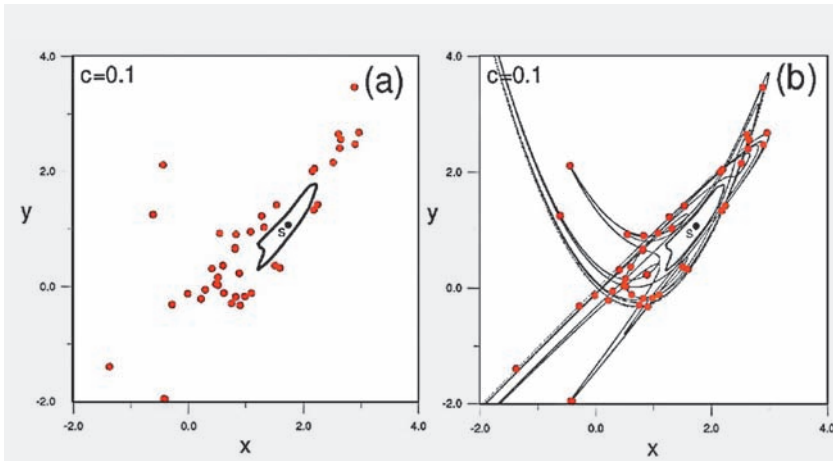


Figure 7: The invariant curves in the variables  $\xi, \eta$ , are hyperbolae  $\xi\eta = c$ . The blue curves 1-4 correspond to the invariant curves of Fig. 6b. The red curves mark the limits of convergence. Any point A has a pre-image B and an image C on the same Moser curve.

ing value  $c = c_{max}$  forms a small closed curve around  $S$  (Contopoulos and Harsoula 2015).

On the other hand, around the point  $S$  there are invariant KAM curves, which are given by formal series, and higher order stable and unstable periodic orbits. Near these unstable orbits there are small chaotic regions, where the KAM theorem does not apply. But the Moser formulae are valid also in the region between the last KAM curve and the limiting Moser curve around  $S$ . Therefore the Moser series do not converge.



**Figure 8:** The images of two points (red) starting on the curve  $c = 0.1$  for  $k = 1.43$  seem to be random (a), but they are all in the same black curve (b).

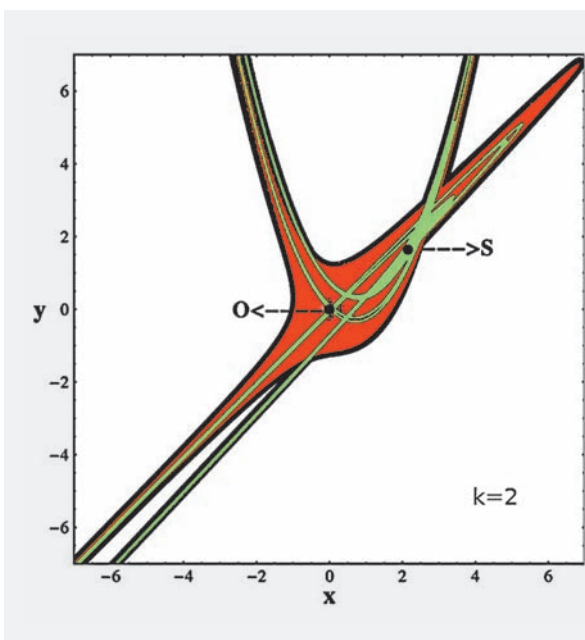


**Figure 9:** The domain of convergence of the Moser series around  $S$  for  $k = 2$  (green) is inside the domain of convergence around  $O$  (red).

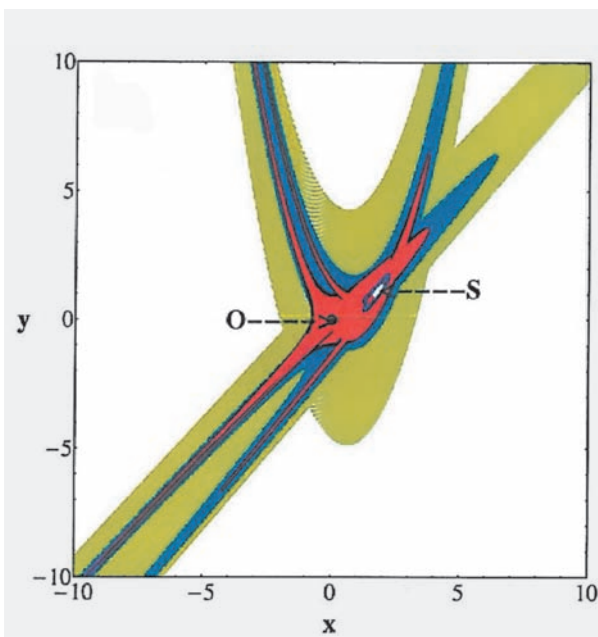


**Figure 10:** Orbits starting in the region  $(-10 < x < 10, -10 < y < 10)$  (for  $k = 1.43$ ) outside the domain of convergence (red) have their first images and pre-images in the green region and their second images and pre-images in the blue region, approaching the boundary of the region of convergence.

For larger values of  $k$  the stable point  $S$  becomes unstable. Then the point  $S$  has its own asymptotic curves and we can again find a transformation of variables (different from the variables  $\xi, \eta$  around  $O$ ) and a domain of Moser curves. This domain of convergence is completely inside the domain of convergence of the Moser curves around  $O$  (Contopoulos and Harsoula 2015) (Fig. 9).

In this case the successive iterates of a point close to the last KAM curve around  $S$  can be given by Moser series around  $O$  and also by Moser series around  $S$ .

In particular, by using the Moser series we could find various periodic orbits, stable and unstable, around  $S$ . We could also find analytically the homoclinic points where the asymptotic curves from the central unstable orbit  $(0, 0)$  intersect. It is even more interesting that we could find analytically the intersecting points between the asymptotic curves from  $O$  and from  $S$  when the periodic orbit  $S$  is unstable (heteroclinic points) (Contopoulos and Harsoula 2015).

When we calculated orbits outside the convergence domain we found a strange result (Contopoulos and Harsoula 2015). Namely the orbits tend to come close to the limiting curves of the convergence of the Moser series (Fig. 10). Therefore, we can find approximately the higher order points of orbits beyond the limits of convergence of the Moser series.

We conclude that many characteristics of the chaotic orbits can be found analytically by using the Moser formulae.

Applications of the Moser formulae in particular dynamic systems have given interesting results. We calculated analytically chaotic spiral arms of barred galaxies (Harsoula et al. 2016) and the spiral arms of galaxies with more than one pattern speeds (Efthymiopoulos et al. 2020). In particular we found the spirals of a barred galaxy when the spirals rotate with an angular velocity  $\Omega_s$ , different from that of the bar  $\Omega_b$ . In this case the spirals vary recurrently in time with a period

$$T = \frac{\pi}{|\Omega_b - \Omega_s|}.$$

These results are consistent with numerical simulations.

### 3. Integrals in relativity, cosmology and quantum mechanics

Formal integrals in relativity were found around 1990 (Contopoulos 1990, 1991). In particular, the periodic problem of 2 fixed black holes has both order and chaos (Chandrasekhar 1989). While most orbits escape chaotically to infinity, there are also regions around stable periodic orbits where the orbits are ordered (Fig. 11). Further work on order and chaos in general relativity was done after these first papers (see, a.g. the symposium on "Deterministic Chaos in General Relativity" (Hobil et al. 1994)). In cosmology much work was done on the "mixmaster" model of the universe (Belinski and Khalatnikov 1959, Misner 1969, etc.). This model has the Hamiltonian

$$H = \frac{1}{2} (p_x^2 + p_y^2 - 2p_x p_y - 2p_y p_z - 2p_z p_x) + e^{2x} + e^{2y} + e^{2z} - 2e^{x+y} - 2e^{y+z} - 2e^{z+x} = 0 \quad (10)$$

and its energy is zero.

The orbits of this model have zero Lyapunov characteristic number, and thus it was suspected that this system is integrable. However, it was shown (Latifi et al. 1994, Contopoulos et al. 1965) that the Mixmaster model is not integrable. Its LCN is zero because all the orbits escape to infinity. Thus this model is "chaotic scattering".

As regards integrals in quantum mechanics, the orbits that are found by solving Bohm's equations (Bohm 1952a,b)

$$\dot{\vec{r}} = \text{Im} \left( \frac{\nabla \psi}{\psi} \right), \quad (11)$$

(where  $\psi$  is a solution of Schrödinger's equation and  $\text{Im}$  stands for the imaginary part), most orbits are chaotic. However, there are also many cases with ordered orbits. In the general case when the wavefunction  $\psi$  corresponds to the classical potential of two harmonic oscillators  $V = \frac{1}{2} (\omega_1^2 x^2 + \omega_2^2 y^2)$  all the orbits are periodic if  $\omega_1/\omega_2$  is a rational number. But if  $\omega_1/\omega_2$  is irrational ordered and chaotic orbits coexist.

In the particular case with  $\omega_1 = 1$

$$\psi = \exp(-(x^2 + \omega_2 y^2) - i(1 + \omega_2)t) \times (1 + axe^{-it} + b\omega_2^{1/2}xye^{-i(1+\omega_2)t}), \quad (12)$$

(Parmenter and Vallentine 1995) (Fig.12) the chaotic orbits approach, from time to time, a nodal point, where

$$\psi = \psi_R + i\psi_{Im} = 0,$$

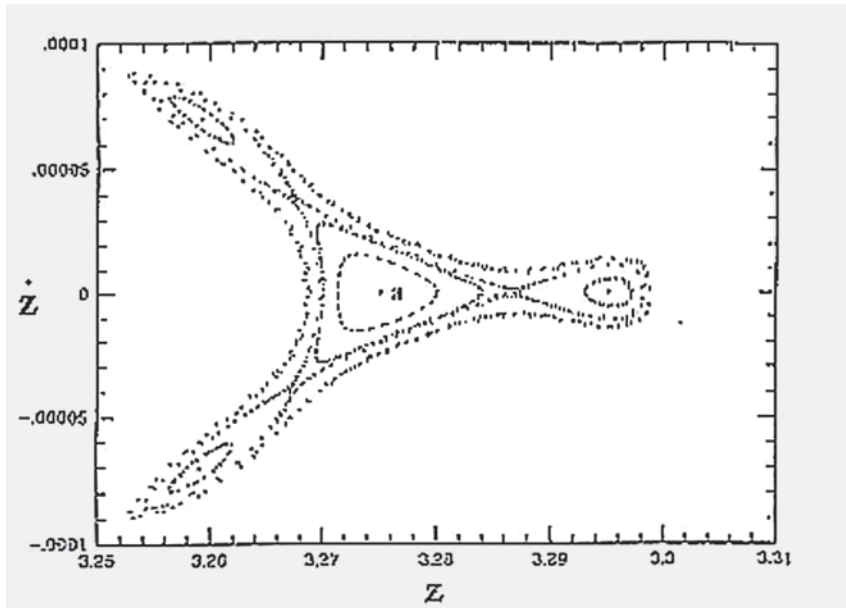


Figure 11: Invariant curves around stable periodic orbits on a surface of section in the problem of two fixed black holes. Close to the 3 unstable periodic orbits and outside the outer invariant curves the orbits are chaotic.

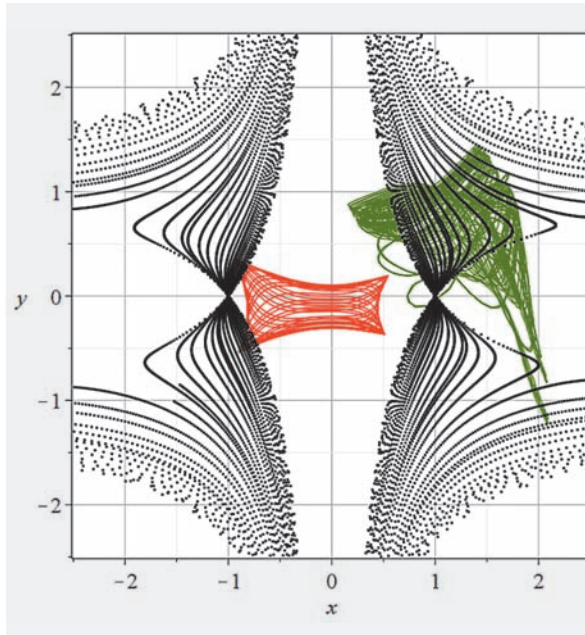


Figure 12: A chaotic Bohmian trajectory (green, right) and an ordered Bohmian trajectory (red, center), together with the trajectory of the nodal point (black dotted curves).

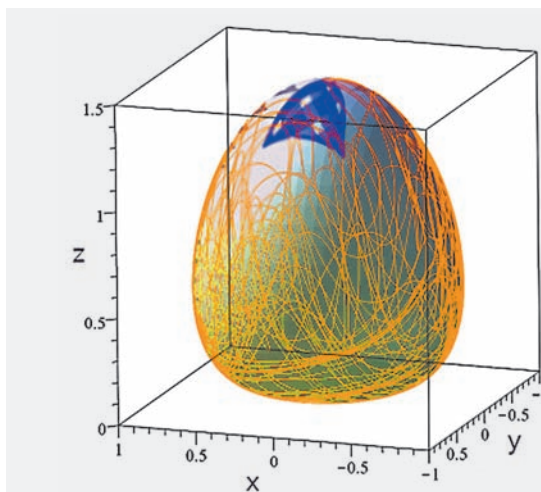


Figure 13: An ordered orbit (blue) and a chaotic orbit (orange) on a pear shaped surface of a partially integrable quantum system.

while the ordered orbits never approach the nodal point. In Fig. 12 we show the orbit of the nodal point (black) and two orbits, one ordered (red) and one chaotic (green). The ordered orbit is a “box orbit” which is similar to a Lissajous curve. This can be given approximately by a series of the form of the third integral (Efthymiopoulos et al. 2007) when the constants  $a$  and  $b$  are small, even if the box containing the orbit is very different from a parallelogram. Much work has been done in recent years on the Bohmian orbits in two and three dimensions (see the review of Contopoulos and Tzemos (2020)).

In particular we have found 3-d cases of wave functions (time dependent) that have an integral of motion, thus they are partially integrable. In these systems the orbits evolve on an integral surface. In the case of Fig. 13 we see an ordered and a chaotic orbit (blue and red respectively). In this case the wavefunction (solution of the Schrödinger equation) is (Contopoulos et al. 2017, Tzemos and Contopoulos 2018)

$$\Psi = \frac{1}{\sqrt{3}}(\Psi_{1,0,0} + \Psi_{0,1,0} + \Psi_{0,0,2}) \quad (13)$$

where  $\Psi_{n_1, n_2, n_3}$  are partial solutions with quantum numbers  $n_1, n_2, n_3$ . The inte-

gral surface in this case is pear-shaped

$$x^2 + y^2 + z^2/2 - \frac{\sqrt{3} \ln(z)}{6} = C. \quad (14)$$

There are many similar partially integrable cases, but there are also cases which are completely integrable, or completely chaotic (with no integral).

Therefore the theory of the third integral can be extended in many cases. Further details can be found in review papers like (Contopoulos 2020).

## References

- Arnold, V. I., 1961, Doklady USSR, **137**, 255  
 Belinski, V.A., & Khalatnikov, I.M., 1969, Sov. Phys. JETP, **29**, 911.  
 Bohm, D., 1952a, Phys. Rev., **85**, 166,  
 Bohm, D., 1952b, Phys. Rev., **85**, 189.  
 Chandrasekhar, S., 1989, Proc. Roy. Soc. London A, **421**, 227.  
 Cherry, T.M., 1924a, Math. Proc. Cambridge Phil. Soc., **22**, 273  
 Cherry, T.M., 1924b, MNRAS, **84**, 729.  
 Cherry, T.M., 1928, Proc. London Math. Soc., **27**, 151.  
 Chirikov, B.V., 1979, Phys. Rep. **52**, 263.  
 Contopoulos, G., 1958, Stockholm Obs. Ann., **20**, 5.  
 Contopoulos, G., 1960, Z. Astrophys., **49**, 273.  
 Contopoulos, G., 1965, Astron. J. **70**, 526.  
 Contopoulos, G., 1966a, IAU Symposium, **25**, 3.  
 Contopoulos, G., 1966b, Astrophys. J. Suppl., **13**, 503.  
 Contopoulos, G., 1966c in Hénon, M. & Nahon, F. (eds), “Les nouvelles méthodes de la dynamique stellaire”, Bull. Astron. (3), **2**, 223 (1967).  
 Contopoulos, G., 1990, Proc. Roy. Soc. London A, **431**, 183  
 Contopoulos, G., 1991, Proc. Roy. Soc. London A, **435**, 551.  
 Contopoulos, G., 2002, Order and Chaos in Dynamical Astronomy, Springer Verlag.  
 Contopoulos, G., 2020, Math. Eng., **2**, 472.  
 Contopoulos, G., & Harsoula, M., 2015, J. Phys. A, **48**, 335101.  
 Contopoulos, G., & Tzemos, A.C., 2020, Reg. Chaotic. Dyn., **25**, 476.  
 Contopoulos, G., Efthymiopoulos, C., & Giorgilli, A. 2003, J. Phys. A, **36**, 8639.  
 Contopoulos, G., Galgani, L., & Giorgilli, A., 1978, Phys. Rev. A, **18**, 1183.  
 Contopoulos, G., Grammatikos, B., & Ramanani, A., 1965, J. Phys. A, **28**, 5313.  
 Contopoulos, G., Tzemos, A.C., & Efthymiopoulos, C., 2017, J. Phys. A, **50**, 195101.  
 da Silva Ritter, G.I., de Almeida, A.M.O., & Douady, R., 1987, Physica D, **29**, 181.  
 de Almeida, A.M.O., & Vieira, W.M., 1997, Phys. Lett. A, **227**, 298.  
 Efthymiopoulos, C., 2005, Cel. Mech. Dyn. Astron., **92** 29.  
 Efthymiopoulos, C., Giorgilli, A., & Contopoulos, G., 2004, J. Phys. A, **37** 10831.  
 Efthymiopoulos, C., Harsoula, M., & Contopoulos, G., 2020, Astron. Astrophys., **636**, A44.  
 Efthymiopoulos, C., Kalapotharakos, C., & Contopoulos, G., 2007, J. Phys. A, **40**, 12945.  
 Giorgilli, A., 1979, Computer Phys. Commun., **16**, 331.  
 Giorgilli, A., 2001, Discrete Cont. Dyn. Syst., **7**: 855.  
 Gustavson, F.G. 1966, Astron. J., **71**, 670.  
 Harsoula, M., Efthymiopoulos, C., & Contopoulos, G., 2016, MNRAS, **459**, 3419.  
 Hobill, D., Burd, A. & Coley, A. (eds), 1994, Deterministic chaos in general relativity, Plenur Press, N. York  
 Hénon, M., & Heiles, C., 1964, Astron J. **69**, 73.  
 Kaluza, M., & Robnik, M., 1992, J. Phys. A, **25**, 5311.  
 Kolmogorov, A.N., 1954, Dokl. Akad. Nauk SSSR, **98**, 527.  
 Latifi, A., Musette, M., & Conte, R., 1994, Phys. Lett. A, **194**, 83.  
 Lynden-Bell, D., 1962, MNRAS, **123**, 447.  
 Misner, C.M., 1969, Phys. Rev. Lett., **22**, 1071.  
 Moser, J., 1956, Commun. Pure Appl. Math., **9**, 673.  
 Moser, J., 1958, Commun. Pure Appl. Math, **11**, 81. 257.  
 Moser, J., 1962, Nachr. Acad. Wiss. Göttingen, **11**, 1.  
 Nekhoroshev, N.N., 1977, Russ. Math. Surv., **32**, 5.  
 Ollongren, A., 1962, Bull. Astron. Neth. **16**, 241.  
 Parmenter, R. H., & Valentine, R. W., 1995, Phys. Lett. A, **201**, 1.  
 Rosenbluth, M.N., Sagdeev, R.A., Taylor, J.B., & Zaslavsky, G.M., 1966, Nucl. Fusion **6**, 253.  
 Tzemos, A.C., & Contopoulos, G., 2018, J. Phys. A, **51**, 075101.  
 Tzemos, A.C., & Contopoulos, G., 2020, Regul. Chaotic Dyn., **26**, 89.  
 Tzemos, A.C., & Contopoulos, G., 2021, Physica D, **419**, 132847.  
 Whittaker, E.T., 1916, Proc. Roy. Soc. Edinburgh, **37**, 95.  
 Whittaker, E.T., 1937, A Treatise on the Analytical Dynamics of Particles and Rigid Bodies, 4 Eds., Cambridge University Press.  
 Vieira, W.M., & de Almeida, A.M.O., 1996, Physica D, **90**, 9.

# Episodic Mass Loss in Evolved Massive Stars

by Alceste Z. Bonanos

IAASARS, National Observatory of Athens, Penteli 15236, Greece

## Introduction

The role of mass loss from massive stars, especially episodic mass loss in evolved massive stars, is one of the outstanding open questions facing stellar evolution theory (Smith 2014). While the upper limit to the masses of stars is thought to be  $150 M_{\odot}$  (Figer 2005; Oey & Clarke 2005), and was even claimed to exceed  $300 M_{\odot}$  (Crowther et al. 2010; Banerjee et al. 2012; Brands et al. 2022; Kalari et al. 2022), the masses of hydrogen-deficient Wolf-Rayet (WR) stars do not exceed  $20 M_{\odot}$  (Crowther 2007). Classical line-driven wind theory (Kudritzki & Puls 2000), once thought to be responsible for removing the envelopes of massive stars, has been shown inadequate, both on theoretical grounds (due to clumping, Owocki & Puls 1999) and estimations based on spectral lines (Bouret et al. 2005; Fullerton et al. 2006; Cohen et al. 2014), which demand reductions in the mass-loss rates by a factor of  $\sim 2$ -3. So how do massive stars shed their envelopes? Binary interactions via Roche-Lobe overflow (RLOF) are predicted to occur in 70% of massive stars and strip the envelopes in  $\sim 30\%$  of O stars, given the high binarity fraction ( $\sim 70\%$ ) of massive stars (Sana et al. 2012). Episodic mass loss is possibly the dominant process that operates in single stars, however, the physical mechanism responsible remains a mystery (Smith 2014).

The importance of episodic mass loss has come to the forefront in both the massive star and supernova (SN) communities. *Spitzer* images have revealed numerous circumstellar shells surrounding massive, evolved stars in our Galaxy (Gvaramadze et al. 2010; Wachter et al. 2010). Episodes of enhanced mass loss have been recorded not only in luminous blue variables (LBVs), but also in extreme red supergiants (RSGs, e.g. VY CMa; Decin et al. 2006, Dupree et al. 2022). Moreover, untargeted supernova surveys have found dusty circum-

stellar material around superluminous supernovae (SLSN, Gal-Yam 2012), and mysterious optical transients with luminosities intermediate between novae and supernovae. The presence of circumstellar material implies a central role of episodic mass loss in the evolution of massive stars and this proposal aims to confirm this hypothesis. Tantalizing evidence suggests that SLSN occur in low-metallicity host galaxies (Neill et al. 2011; Gal-Yam 2019), implying that such supernovae dominated the metal-poor early Universe. The overluminous Type IIIn SN 2010jl is a well-studied example of a SLSN, with a massive progenitor star ( $30 M_{\odot}$ ) surrounded by a dense circumstellar shell (Smith & Frew 2011; Zhang et al. 2012), which exploded in a low-metallicity galaxy (Stoll et al. 2011). SN2008S, a well-studied example of the class of intermediate-luminosity optical transients, was found to have a dust-enshrouded progenitor ( $8$ - $10 M_{\odot}$ , Prieto et al. 2008) in pre-explosion *Spitzer* images of the host galaxy NGC 300. Finally, the remarkable SN2009ip involves a  $50$ - $80 M_{\odot}$  progenitor that underwent a series of episodic mass loss events. Its spectacular finale included a series of eruptions in 2009 and 2010 until its final explosion in 2012 as a Type IIIn supernova (Mauerhan et al. 2013; Smith et al. 2022). These examples strongly suggest that episodic mass loss in massive stars is central to their evolution and therefore has profound consequences for the enrichment of the interstellar medium and the chemical evolution of the early Universe.

The physics of LBV eruptions, pre-SN eruptions and extreme RSG mass-loss is still in its infancy and, as stated in the review by Smith (2014), “is a major unsolved problem in astrophysics”. Models of single-star evolution adopt empirical, constant mass-loss prescriptions (Meynet et al. 2015; Beasor et al. 2021) or, recently, time-averaged mass-loss rates (Massey et al. 2023), which highly influ-

ence the outcome. There have also been recent improvements in the methodology of measuring RSG mass loss rates vs. luminosity, however, the resulting mass loss rates differ significantly (Beasor et al. 2020; Decin et al. 2023).

## ASSESS project

The ASSESS project<sup>1</sup> (ERC grant No. 772086; PI Bonanos, 2018-2024) tackles the role of episodic mass loss in massive stars by using the fact that mass-losing stars form dust and are bright in the mid-infrared (mid-IR). Physically, there are a number of ways a massive star can become a source of significant mid-IR emission. First, dust can form in a dense, but relatively steady stellar wind. In the most extreme cases, such as in the progenitors of the SN 2008S and the NGC300-OT 2008 transient (Bond et al. 2009), the wind is optically thick even in the near-IR and the source star is seen only in the mid-IR (Prieto et al. 2008). Second, a very massive star can have an impulsive mass ejection or eruption with dust forming in the ejected shell of material. Initially the optical depth and dust temperatures are high, but then drop as the shell expands. The most famous example is the “great eruption” of  $\eta$  Carinae in the 19<sup>th</sup> century (Humphreys & Davidson 1994; Davidson & Humphreys 1997; Smith & Frew 2011), which ejected several solar masses of material. Third, the dust can be in a circumstellar disk and emit over a broad range of temperatures, as is seen in supergiant B[e] stars (sgB[e] stars (Zickgraf 2006).

While stars with significant mid-IR emission are intrinsically rare, many of the most interesting massive “superstars”, such as  $\eta$  Car or “Object X” in M33 (Khan et al. 2011, Mikolajewska et al. 2015), belong to this class. Searching for analogs of these interesting stars using mid-

1. <http://assess.astro.noa.gr/>

IR photometry of nearby galaxies is the way to go. The existing mid-IR “road-maps” for interpreting luminous massive stars (Bonanos et al. 2009, 2010) are based on known massive stars in the LMC and the SMC. They have identified LBVs, sgB[e], and RSGs among the brightest mid-IR sources, due to their intrinsic brightness and due to being surrounded by their own dust.

The ASSESS team<sup>2</sup> aims to determine whether episodic mass loss is a dominant process in the evolution of the most massive stars. What is new about ASSESS is the idea of conducting – for the first time – a systematic study of mass loss in massive stars, by selecting targets using mid-IR photometry of nearby galaxies obtained with *Spitzer*. We aim to derive physical parameters of ~1000 dusty, evolved massive stars in ~25 nearby galaxies and estimate the amount of ejected mass, which will constrain evolutionary models. We present the methodology and first results of the project, including the machine-learning algorithm for target selection, results from our spectroscopic observations, our newly derived mass loss rates for red supergiants, at low metallicity, and the implications of the latter on stellar evolutionary models. The emerging trend for the ubiquity of episodic mass loss, if confirmed, will be key to understanding the explosive early Universe and will have profound consequences for low metallicity stars, reionization, and the chemical evolution of galaxies.

## Methodology

We have collected recently published mid-IR photometric catalogs from *Spitzer* of galaxies with high star-formation rates within 5 Mpc:

- seven dwarf galaxies within 1.5 Mpc from the DUSTINGS project (Boyer et al. 2015): IC 10, IC 1613, Phoenix, Pegasus, Sextans A, Sextans B, and WLM,
- 13 galaxies within 5 Mpc (Khan et al. 2015; Khan 2017): M31, M33, NGC 247, NGC 300, NGC 1313, NGC 2403, M81, M83, NGC 3077, NGC 4736, NGC 4826, NGC 6822, and NGC 7793, and

2. Team members include Kostas Antoniadis, Evangelia Christodoulou, Stephan de Wit, Grigoris Maravelias, Gonzalo Munoz-Sanchez and Manos Zapartas. Frank Tramper and Ming Yang are former members.

- five galaxies within 4 Mpc (Williams & Bonanos 2016): NGC 55, NGC 253, NGC 2366, NGC 4214, and NGC 5253.

The mid-IR photometry made available by the SAGE surveys of the LMC (Meixner et al. 2006) and SMC (Gordon et al. 2011) has been also searched for undetected, dust-obscured targets in our nearest neighbor galaxies. These catalogs contain mid-IR photometry of over 5 million point sources in 27 nearby galaxies, 19 of which have Pan-STARRS1 coverage (Chambers et al. 2016), providing an ideal dataset for a systematic study of luminous, dusty, evolved massive stars. We have compiled mid-IR photometric catalogs for these galaxies, including their counterparts in Pan-STARRS1, 2MASS (Cutri et al. 2003), VISTA Science Archive, WISE (Cutri & et al. 2012) and other archival surveys of particular galaxies to construct their spectral energy distributions (SEDs) out to 24  $\mu\text{m}$ .

Based on these catalogs, we have selected over 1000 luminous and red sources (selected by their colors in [3.6] – [4.5]) in these 27 galaxies and are conducting follow-up low-resolution spectroscopy of these sources, mainly with FORS2 on VLT and OSIRIS on GTC. The spectra yield stellar types, luminosity classes, effective temperatures and an estimate of the reddening. High-resolution spectra are being obtained for particularly interesting targets for further analysis.

SED modeling with the radiative transfer code DUSTY (Ivezic & Elitzur 1997) is providing radii and age estimates of the circumstellar shell, as well as the dust temperature, ejected mass, and bolometric luminosity. SED shapes will be quantified to estimate the timescales of episodic mass loss and lifetimes of the various evolved stages as a function of spectral type and metallicity. Evidence of binarity (from spectra, SEDs, light curves) will provide an estimation of the relative contribution of RLOF to the observed dusty evolved stages of massive stars. Armed with all these parameters for a sample of ~1000 dusty, evolved stars, spanning a range of metallicity (~1/15 – 2  $Z_{\odot}$ ), we will perform a comparison with state-of-the-art stellar evolutionary models (Brott et al. 2011; Ekstroem et al. 2012; Georgy et al. 2013; Meynet et al. 2015) to evaluate the input mass-loss rates and predicted out-

comes. We plan to reverse-engineer the target stars to quantify and confirm the amount of “input” episodic mass loss needed to match the measurements.

## Results

### i) Photometric classifier

We have employed state-of-the-art machine-learning algorithms to automatically classify and select types of mass-losing stars, thereby accelerating and systematizing the investigation of multi-wavelength photometry. We developed a classifier for evolved massive stars based on known massive stars in M31 and M33 and using color indices as features to classify evolved massive stars into the following categories: blue, yellow, red supergiants, LBVs, classical Wolf-Rayet stars, sgB[e]. We also included a class for outliers (e.g. background galaxies, AGNs). The classifier is found to be on average 83% accurate (Maravelias et al. 2022). We have applied this classifier to classify over one million sources in 25 nearby galaxies (Maravelias et al. 2023, in prep.), which we will be useful for many other studies.

### ii) Observational survey

The targets were prioritized based on their luminosity and IR excess, specifically, targets with  $m_{3.6} - m_{4.5} \geq 0.5$  mag and  $M_{3.6} \leq -9.75$  mag had highest priority. We have obtained multi-object spectroscopy with both the VLT and GTC starting in 2020, giving priority to the galaxies that had enough high-priority targets to justify multi-object spectroscopy. We used the FORS2 spectrograph (Tramper et al., in prep.) and obtained spectra of over 400 high-priority and over 500 “filler” stars in M83, NGC 55, NGC 247, NGC 253, NGC 300, NGC 7793, Sextans A and WLM over 43h. The spectra have a resolving power of  $R = 1000$  and a wavelength coverage around 5400–8200 Å, which is suitable for classification and parameter estimation. From the VLT data, we have so far classified over 360 massive, evolved stars, including:

- 6 sgB[e] stars of which 5 are new discoveries (Maravelias et al. 2023),
- 5 LBV candidates, of which 3 are new discoveries (see Fig. 1; Maravelias et al. 2023),
- 130 red supergiants (mainly new discoveries in low metallicity galaxies, de Wit et al., in prep.).

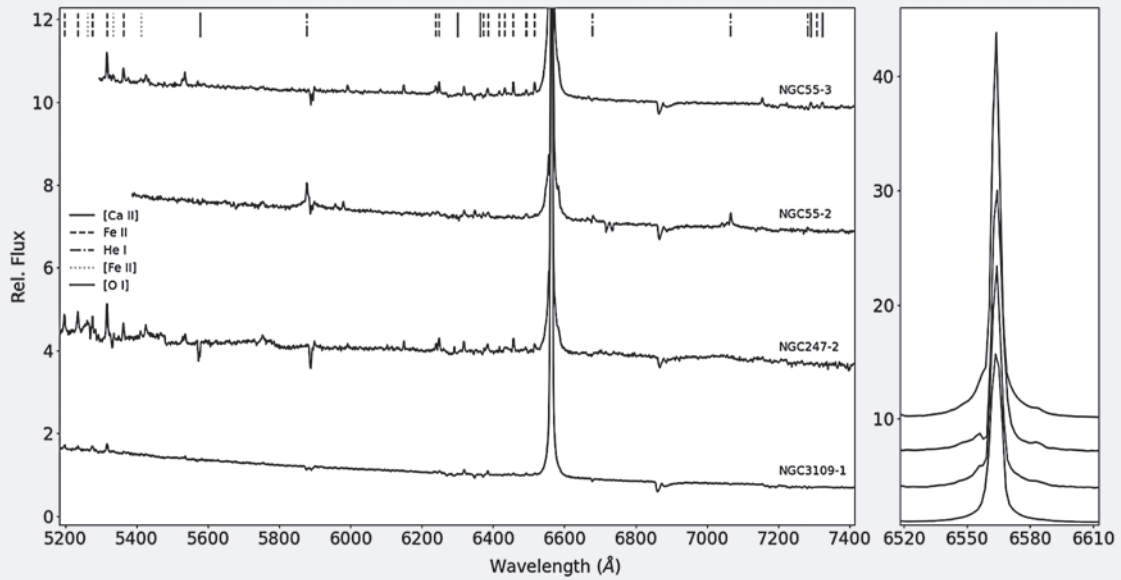


**Figure 1:** Spectra of new LBV candidates (Maravelias et al., *subm.*). Left: The full spectra for all stars with small offsets for better illustration purposes. The most prominent emission features are indicated. Right: The region around H $\alpha$  is highlighted to emphasize the relative strength of the emission compared to the continuum.

Higher-resolution spectra will be obtained to model the LBV candidates, while MARCS modeling will yield parameters of the RSG. Figure 2 presents the spatial distribution of the classified targets in NGC 300. Additional spectra of ~200 sources in dwarf galaxies are scheduled for the spring/summer 2023.

We also used the GTC OSIRIS spectrograph and have so far obtained spectra of 48 high-priority stars in NGC 6822 and 33 in IC 10, with 600 additional spectra of sources in NGC 2403, M81, NGC 4214, NGC 4736, NGC 2366, Sextans B, NGC 3077 scheduled in semester 2023A. The GTC spectra have a resolving power of  $R \sim 500-700$ , a wavelength coverage around 5200–9200 Å, and are being used to classify the sources and obtain their parameters (Munoz-Sanchez et al., *in prep.*). Higher-resolution near-infrared spectra with EMIR on GTC have also been obtained for a sample of ~10 RSG (see Fig 2), for which we are performing MARCS model fitting to derive their parameters and particularly  $T_{\text{eff}}$ .

In the Magellanic Clouds, we have similarly selected dusty, evolved sources and obtained spectra with the MagE spectrograph on Magellan and identified 8 new RSGs. Among them is a luminous, extreme RSG, with similar properties to WOH G64. We also identified a new LBV candidate. Our results are presented by de Wit et al. (2023).

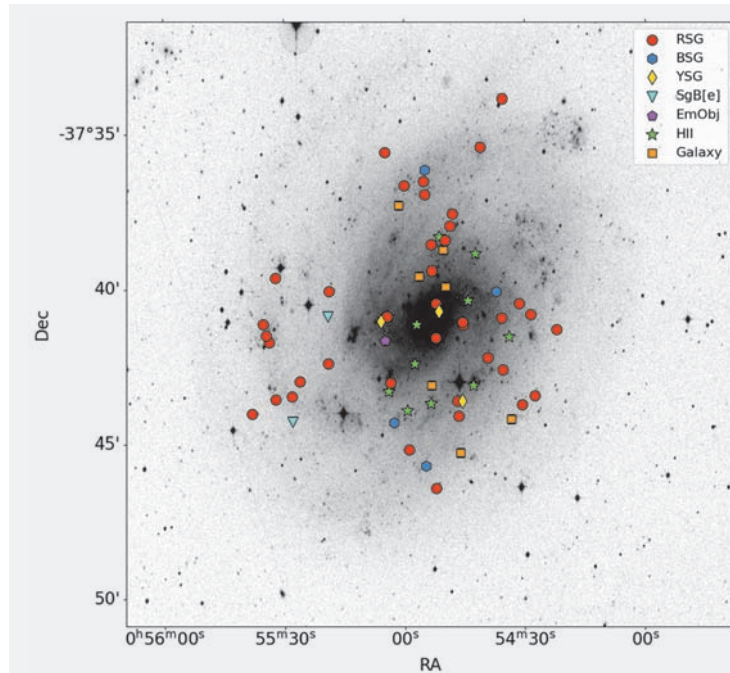


**Figure 2:** Spatial distribution of classified targets from our survey of dusty, evolved sources in NGC 300. The background image is from the Digitized Sky Survey (Tramper et al., *in prep.*).

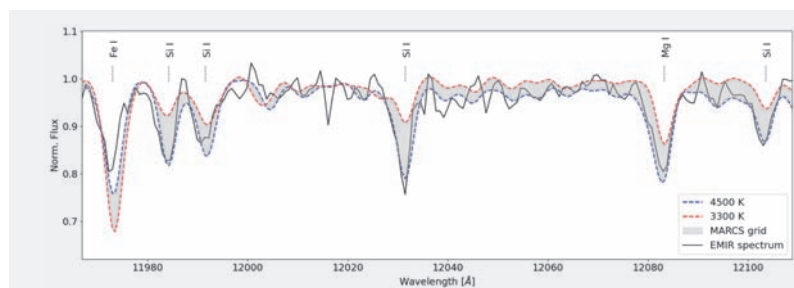


**Figure 3:** Example of a reduced, telluric-corrected GTC/EMIR spectrum of a RSG in IC 10, with a grid of MARCS models overplotted, illustrating the sensitivity of the J-band to  $T_{\text{eff}}$ .

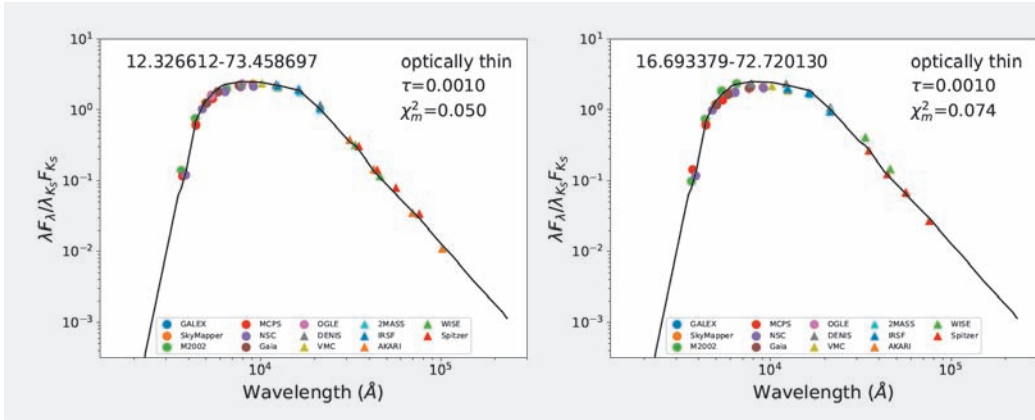


**Figure 4:** Examples of the DUSTY fitting of RSG in the SMC (from Yang et al. 2023). Similar work is underway for the LMC (Antoniadis et al., in prep.).

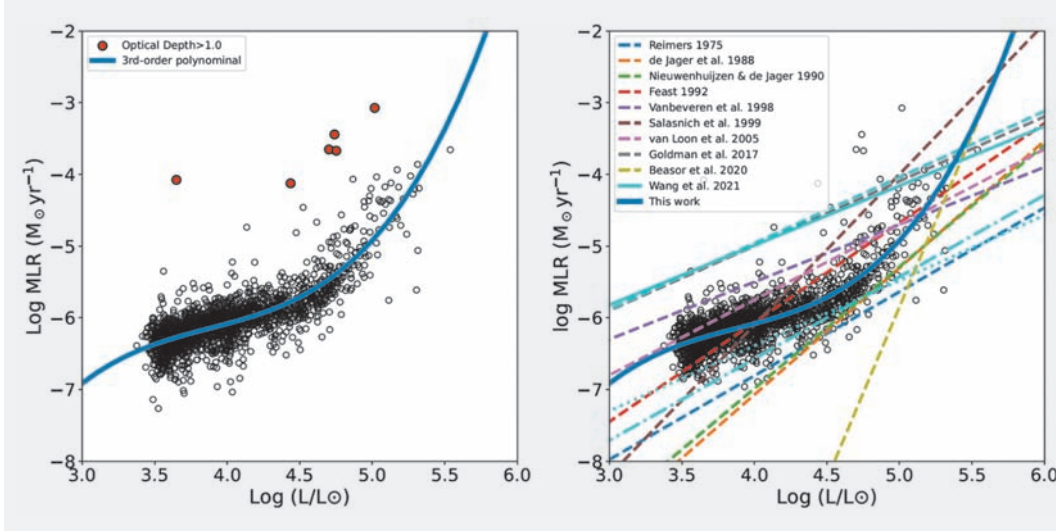


**Figure 5:** Derived MLR-L relation from Yang et al. (2023) and comparison of the same relation with previous works (right). In the left panel, the very dusty targets ( $\tau_v > 1$ ) are marked with red colors. In the right panel, lines of the same color are variations of the same relation.

### iii) Mass loss rates

We have determined the mass loss rates (MLR) of red supergiants in the Small Magellanic Cloud, based on the catalogs of Yang et al. (2020) and Ren et al. (2021). Comprehensive photometry in over 50 bands (from the UV to 24 $\mu$ m) for over 2,000 RSG has been compiled and a grid of DUSTY models (Ivezic & Elitzur 1997) was created for silicate dust. This grid was used to perform a  $\chi^2$  fit of the SEDs (see Fig. 4) and determine the dust parameters, optical depth and the mass loss rate for each supergiant. From the distribution of MLR, we find a typical value of  $\sim 10^{-6} M_{\odot} \text{ yr}^{-1}$ , with a few outliers at around  $\sim 10^{-4}$  and  $10^{-3} M_{\odot} \text{ yr}^{-1}$ . We determine a new MLR vs. L relation based on an unbiased sample of RSG in the SMC, which shows an upturn at around  $\log(L/L_{\odot}) = 4.6$ , with enhanced mass loss occurring at higher L (see Fig. 5). Compared to previously determined relations in the SMC, our result (Yang et al. 2023, A&A, in press) is most similar to the relations of Feast (1992) and van Loon et al. (2005). We find a similar result for the RSG of the LMC (Antoniadis

et al., in prep.), with a similar upturn at high luminosities. The procedure will be applied to the rest of our program galaxies to determine the mass-loss rate (MLR) at a range of metallicities and its metallicity dependence.

### iv) Stellar evolutionary models

We are investigating the effect of these new and measured mass-loss rate prescriptions as well as others from literature on stellar evolutionary models, and in particular MESA models (e.g., Paxton et al. 2011). We have implemented the mass loss rate prescription of Yang et al. (2023, see Figure 5) on a grid of single star models of SMC metallicity, ( $Z \sim 0.3 Z_{\odot}$ ), that follows the assumptions of the population synthesis code POSYDON (Fragos et al. 2023). We compare the theoretical predicted surface properties of the RSGs with the observed ones (e.g. their position in the Hertzsprung-Russell diagram, Figure 6). We find that the high mass-loss rate of the Yang et al. prescription leads to extreme stripping of the envelope of the RSGs, leaving only a thin Hydrogen-rich layer above

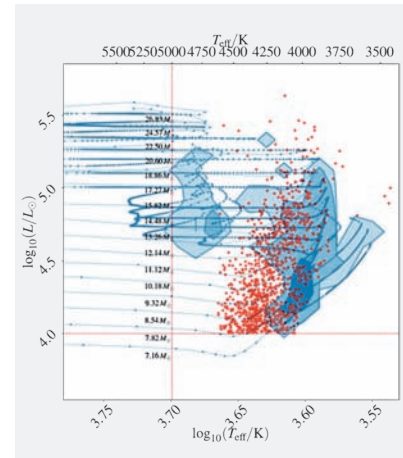


**Figure 6:** Hertzsprung-Russell diagram of the stellar evolution models. The blue contours show the expected positions of RSGs that lose mass according to the prescription of Yang et al., with 0.68, 0.95, 0.99 probability as we go to darker colors. Stellar tracks of various initial masses are also shown, with blue points of equal timestep of  $10^3$  years. The red dots depict the largest observed sample of RSGs in the SMC, compiled from Yang et al. 2020 and Ren et al. 2021. We conservatively consider a star to be in its RSG phase if it is more luminous than  $10^4 L_{\odot}$ , and below 5,000 K.

their cores, driving them to hotter temperatures before their eventual death in a supernova.

## Summary

The systematic study of evolved massive stars in nearby galaxies by ASSESS, has led to the development of a photometric classifier based on machine-learning techniques and has yielded classifications of over 360 evolved stars, including 138 RSG, 6 sgB[e] and 6 LBVs. The sample is expected to double in the next year with the completion of the spectroscopic survey. Spectral modeling along with SED modeling has already yielded the physical parameters of RSG and their mass loss rates. The large samples

available in the Magellanic Clouds are yielding relations of mass-loss rate vs. luminosity, which both show an upturn at high L. Implementing the above results in stellar evolution codes allow us to compare theoretical models with observations, investigating the impact of our results on RSGs and their eventual supernovae.

This survey is timely, given the recent availability of mid-IR catalogs, and ambitious, as it plans to increase the number of evolved massive stars in nearby galaxies by a factor of 5. The James Webb Space Telescope is operating concurrently with this project. The enormous boost in sensitivity and angular resolution will revolutionize our understand-

ing of these nearby objects. However, to fully exploit this we need to be able to tie the JWST results into the more general population. This project provides this anchor. The results of this study will not only provide the first quantitative inventory and characterization of dusty massive stars in 27 galaxies in the nearby Universe at a range of metallicities, but may also reveal new classes of enshrouded stars and rare transitional objects. A byproduct of the survey will be the release of multi-wavelength photometric catalogs of luminous sources in 27 galaxies, including their classifications, which will be valuable for various scientific projects.

## References

- Banerjee, S. et al. 2012, *MNRAS*, 426, 1416  
Beasor, E. et al. 2020, *MNRAS*, 492, 5994  
Beasor, E. et al. 2021, *ApJ*, 922, 55  
Bonanos, A.Z., et al. 2009, *AJ*, 138, 1003  
Bonanos, A.Z., et al. 2010, *AJ*, 140, 416  
Bond, H.E., et al. 2009, *ApJ*, 695, L154  
Bouret, J.-C., et al. 2005, *A&A*, 438, 301  
Boyer, M. et al. 2015, *ApJS*, 216, 10  
Brands, S. et al. 2022, *A&A*, 773, 36  
Brott, I. et al. 2011, *A&A*, 530, 115  
Chambers et al. 2016, *arXiv*, 1612.05560  
Cohen, D.H. et al. 2014, *MNRAS*, 439, 908  
Crowther, P.A. 2007, *ARAA*, 2007, 45, 177  
Crowther, P.A. et al. 2010, *MNRAS*, 408, 731  
Cutri, R.M. et al. 2003, *The IRSA 2MASS All-Sky Point Source Catalog*, NASA/IPAC Infrared Science Archive  
Cutri, R.M. et al. 2012, *WISE All-Sky Data Release*  
Davidson, K. & Humphreys, R.M. 1997, *ARAA*, 35, 1  
De Wit et al. 2023, *A&A*, 669, 122  
Decin, L. et al. 2006, *A&A*, 456, 549  
Decin, L. et al. 2023, *A&A*, subm. (arXiv:2303.09385)  
Dupree, A. et al. 2022, *ApJ*, 936, 18  
Ekstroem, S. et al. 2012, *A&A*, 537, 146  
Feast, M. W. 1992, *Instabilities in Evolved Super- and Hypergiants*, 18  
Figer, D.F. 2005, *Nature*, 434, 192  
Fragos, T. et al. 2023, *ApJS*, 264, 45  
Fullerton, A.W., Massa, D.L., Prinja, R.K. 2006, *ApJ*, 637, 1025  
Gal-Yam, A. 2012, *Science*, 337, 927  
Gal-Yam, A. 2019, *ARAA*, 57, 305  
Georgy, C. et al. 2013, *A&A*, 558, 103  
Gordon, K.D. et al. 2011, *AJ*, 142, 102  
Gvaramadze, V.V. et al. 2010, *MNRAS*, 405, 1047  
Humphreys, R.M. & Davidson, K. 1994, *PASP*, 106, 1025  
Ivezic, Z. & Elitzur, M. 1997, *MNRAS*, 287, 799  
Kalari et al. 2022, *ApJ*, 935, 162  
Khan, R. et al. 2011, *ApJ*, 732, 43  
Khan, R. et al. 2015a, *ApJS*, 219, 42  
Khan, R. et al. 2017, *ApJS*, 228, 5  
Kudritzki, R.-P. & Puls, J. 2000, *ARAA*, 38, 613  
Maravelias et al. 2022, *A&A*, 666, 122  
Maravelias et al. 2023, *Galaxies*, subm.  
Massey, P. et al. 2023, *ApJ*, 942, 69  
Mauerhan et al. 2013, *MNRAS*, 430, 1801  
Meixner, M. et al. 2006, *AJ*, 132, 2268  
Meynet, G. et al. 2015, *A&A*, 575, 60  
Mikolajewska et al. 2015, *ApJ*, 799, 16  
Neill, J.D. et al. 2011, *ApJ*, 727, 15  
Oey, M.S. & Clarke, C.J. 2005, *ApJ*, 620, 43  
Owocki, S.P. & Puls, J. 1999, *ApJ*, 510, 355  
Paxton, B. et al. 2011, *ApJS*, 192, 3  
Prieto, J.L. et al. 2008, *ApJ*, 681, 9  
Ren et al. 2021, *ApJ*, 923, 232  
Sana, H. et al. 2012, *Science*, 337, 444  
Smith, N. et al. 2011, *ApJ*, 732, 63  
Smith, N. 2014, *ARAA*, 52, 487  
Smith, N. et al. 2022, *MNRAS*, 515, 71  
Smith, N. & Frew, D.J. 2011, *MNRAS*, 415, 2009  
Stoll, R. et al. 2011 *ApJ*, 730, 35  
Van Loon et al. 2005, *A&A*, 438, 273  
Wachter, S., et al. 2010, *AJ*, 139, 2330  
Williams, S.J. & Bonanos, A.Z. 2016, *A&A*, 587, 121  
Yang et al. 2020, *A&A*, 639, 116  
Yang et al. 2023, *A&A*, in press (arXiv:2304.01835)  
Zhang, T. et al. 2012, *AJ*, 144, 5  
Zickgraf, F.-J. 2006, *ASP Conference Series*, 355, 135

# Galaxy evolution

## Lessons, challenges, and opportunities in the golden era of observational astrophysics

by Georgios E. Magdis

Cosmic Dawn Center (DAWN), Denmark

DTU-Space, Elektrovej, Building 328, 2800, Kgs. Lyngby, Denmark

Niels Bohr Institute, University of Copenhagen, Jagtvej 128, DK-2200 Copenhagen N, Denmark

**G**alaxies are the building blocks of our Universe. These huge agglomerations of stars, gas and dust, when captured by a powerful observatory like the Hubble Space Telescope (HST), paint some of the most mesmerising pictures known to humanity. But the significance of these inspiring images goes far beyond the aesthetics. Almost everything we know about our cosmic origins stems from the systematic exploration of nearby and distant galaxies. These systems serve as cosmic beacons pinpointing the sites of the mysterious dark matter that surrounds them; they unfold the adventurous history of the Universe that is imprinted in their properties and they echo the processes that shaped the structure of our Cosmos today.

HST and other space and ground-based telescopes have searched and successfully detected the starlight of millions of galaxies across cosmic time, revealing that much like living organisms, galaxies go through various transformations. They grow by converting their gas into stars, they change their chemical composition (when super nova explosions expel metals produced by nuclear fusion in the cores of the stars), they interact with nearby galaxies and they eventually mature and “die” (quench) when they run out of gas and cease to make new stars. These phases in the life cycle of galaxies can be identified in properties of three main classes of galaxies; the *normal disk galaxies* like our Milky Way (MW) that are peacefully converting their gas into stars, the *star-bursting galaxies* (like the local Ultra Luminous Infrared Galaxies) that form stars ten to hundreds of times faster than MW, possible due to a violent merging events that also result in their distorted morphologies, and the *dead passive* or *quiescent galaxies* (QGs) that have stopped

forming new stars. To understand the evolutionary path between these stages and place it into cosmological context, we first need to detect the census galaxies of galaxies across cosmic time, characterise their physical properties and reveal the processes that regulate their formation, their growth and eventually their death.

As the past informs the present, tracing the onset of cycle of galactic life (formation → growth → quenching) back to the early Universe and understanding the nature of the first galaxies in the first billion years of cosmic history is a monumental but also an extremely challenging task for modern astrophysics. When and how do the first galaxies form? How efficiently do they convert their gas to stars? how quickly do they “pollute” the pristine early universe with heavy elements and give rise to the periodic table? What regulates their growth and evolution? What are the physical mechanisms responsible for their death and when do these first come in play?

Obviously, to address these questions, we need to study the various components that make up a galaxy, that to a first order approximation are the baryons in the form of stars, dust and gas, and of course the dark matter halo within which the galaxies reside. Since these components have different observational signatures, tracing the baryonic cycle in galaxies and their dark matter haloes requires multi-wavelength observations that harvest the full electromagnetic spectrum. In this regard, over the last decades the astronomical community has invested copious amounts of time, effort and resources in deep, panchromatic cosmological surveys (e.g. COSMOS, GOODS) that combine observations from the most advanced astronomical facilities, most notably HST and

Spitzer in the UV to mid-IR, Herschel, SCUBA, ALMA and VLA in the far-IR to radio, and of course the JWST in the near to mid-IR that was launched in December 2021 and is already transforming our view of the early Universe. These multi-wavelength synergies have facilitated both the collection of large statistical samples of galaxies that reside at different cosmic epochs, as well as the characterisation of their fundamental properties (e.g. stellar mass –  $M^*$ , star formation rate – SFR, gas mass –  $M_{\text{gas}}$ ), offering snapshots in the timeline of galaxy evolution.

In this review I will attempt to briefly highlight some of the most notable successes of these efforts and discuss the challenges and opportunities in the *golden era* of the study of galaxy evolution that lies ahead.

### The timeline of galaxy evolution

Over the last two decades an avalanche of multiwavelength data from imaging and spectroscopic surveys has revolutionized our understanding of galaxy evolution by tracing both the unobscured (e.g., with HST) and the dust obscured (e.g. with Herschel) star formation in galaxies across cosmic time. These measurements have been used to estimate the total star formation activity in the Universe (in other words the star formation rate density – SFRD), as a function of time, effectively charting the star formation history since the Big Bang (e.g. Madau & Dickinson+14). This has led to the fundamental discovery that the star formation activity, and by proxy the evolution of galaxies, has undergone through various phases and that can be split into three main cosmic epochs (Fig.1); The onset of star and galaxy formation happens soon after the

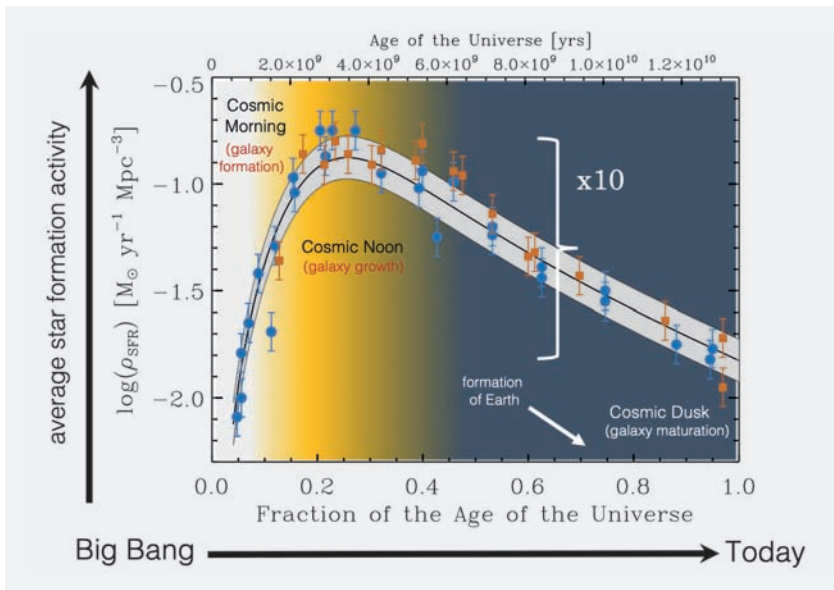


**Figure 1:** The evolution of star formation rate density, The rise, the peak and the gradual decline of the SFRD signifies three distinct epochs in galaxy evolution. The blue and red data points are taken from Madau & Dickinson 2014 and represent measurements of the SFRD using UV-optical and IR SFR *fracers* respectively.

after Big Bang, during the era of “Cosmic Dawn”. In this first 10% of its history the Universe experienced a dramatic increase in its star formation activity, going from being void of structured baryonic matter to making its first stars, first proto-galaxies and eventually first galaxies as we know them today. A couple of billion years later, the Universe entered its most prolific phase; the era of “Cosmic Noon”. During this period, that lasted approximately 4 billion years, galaxies (and their super massive black holes) experienced substantial growth, and produced more than half of the stars that we see today. Finally, the Universe enters the epoch of “Cosmic Dusk”, where over the last 8 billion years, the galaxies mature and die while the overall star formation activity gradually decreases by a factor of 10.

This story that describes the history of the *cosmic metabolism* is justifiably regarded as one of the most fundamental achievements of observational astrophysics. However, describing is not the same as understanding and a new set of pressing questions arises; *what drives the rise, the peak and the decline of the star formation activity in the Universe? how did galaxies assembled their stellar mass? what dictates the baryonic cycle across time?* An approach that has proven to be very efficient in addressing these questions is to establish universal scaling relations and correlations between the fundamental

properties of the galaxies, and explore how these change as a function of time and galaxy type. The emerging “laws” that describe the average behaviour of galaxies then can serve as the test-bed for semi-analytical, hydro-dynamical, and cosmological simulations, eventually bringing us closer to a more comprehensive and more coherent model of galaxy evolution.

### The Main Sequence of Star formation

Two of the most informative physical properties about the evolutionary stage of a galaxy are its star formation rate and its stellar mass. The first indicates the rate at which a galaxy is forming new stars and the second, in essence, reflects the integral of its star formation activity in the past. While accurate  $M^*$  estimates were already possible with HST and Spitzer, a more robust measurement of the SFR in distant galaxies had to wait for the advent of Herschel. Indeed, the spectral coverage (70-500 $\mu$ m) and the sensitivity of Herschel was necessary to probe the dust obscured star formation in distant star forming galaxies (SFGs), that actually dominates the star formation activity during the cosmic noon. Bringing together the  $M^*$  and the revisited SFR estimates, revealed a tight and almost linear relation between the two physical parameters that appears to be followed by 90% of the SFG at

each cosmic epoch (e.g. Noeske+07, Elbaz+07, Magdis+10, Schreiber+15). Galaxies falling below the relation tend to have little or no star formation and are the dead/elliptical quiescent galaxies we discussed before, while the majority of the galaxies that lie above the sequence are undergoing a merger induced starbursts phase experiencing elevated SFRs for the stellar mass.

This *main sequence of star formation* as it has been coined appears to hold over (at least) the last 12 Gyrs with an evolving normalisation factor that increases with redshift mirroring the evolution of the star formation rate density (e.g. Magdis+10,17, Elbaz+11, Schreiber+15).

However, the most intriguing aspect of this relation is it tight and constant scatter of ( $\sigma=0.3$  dex, e.g. Schreiber+15), suggesting that at a fixed  $M_{\text{star}}$  and cosmic time the SFR of 90% of star forming galaxies varies only within a factor of  $\sim 2$ . More importantly, this means that there is a strong memory between the ongoing and the previous star formation activity in the galaxies, a realisation that advocates for a large degree of uniformity in the star formation histories of the galaxies and smooth/secular evolution as the main avenue of galaxy growth. This result came as a great surprise since the high SFRs of the SFGs during the cosmic noon, are almost exclusively associated with short lived, episodic star bursting events in the local Universe. We are thus witnessing a radical change in the star formation mode between near-by and distant galaxies, a realisation that can only be understood by exploring the fuel of star-formation, i.e. the molecular gas reservoir.

### The star formation Law

Understanding the process that leads to star formation on large scales requires measuring the mass and the distribution of the molecular hydrogen ( $M_{\text{H}_2}$ ). However, since  $\text{H}_2$  lacks a dipole moment and typical temperatures in Giant Molecular Clouds are too low to excite quadrupole or vibrational transitions, indirect approaches are required to estimate the molecular gas mass (the  $\text{H}_2$  transition lines in the mid-IR can only trace the warm molecular gas  $T>500\text{K}$  that is only a small fraction of the total  $M_{\text{H}_2}$ ). These proxies of  $M_{\text{H}_2}$  include the dust continuum emission (via the metal-

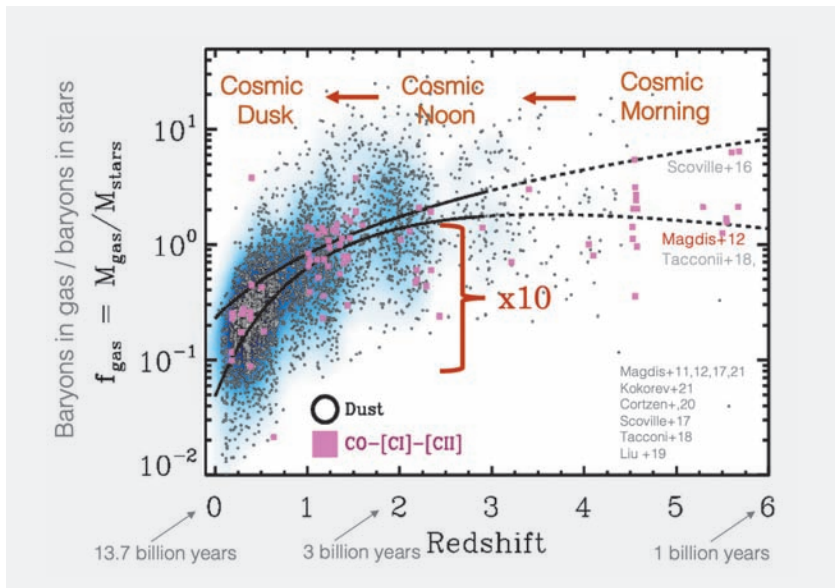


**Figure 2:** The evolution of the gas fraction in star-forming galaxies across cosmic time, using various tracers of H<sub>2</sub>.

licity dependent dust to gas mass conversion method), as well as a range of emission lines of atomic and molecular species that arise from the interstellar medium of galaxies (e.g. CO, [CI], HCN). Targeting these tracers through a series of observational campaigns, Herschel and later ALMA completely revolutionised the field by offering, for the first time, M<sub>H<sub>2</sub></sub> measurements for large statistical samples of galaxies across cosmic time (e.g. Magdis+12,17, Genzel+15, Tacconi+18, Valentino+20).

A key result of these concerted efforts is that the gas to stellar mass ratio, i.e. the gas fraction ( $f_{\text{gas}} = M_{\text{gas}}/M_{\text{star}}$ ) of the galaxies has decreased over that last 10 billion years by the same factor of  $\sim 10$  as the SFRD (Fig.2). Furthermore, the majority of SFGs follow a second tight relation, this time between their SFR and the M<sub>H<sub>2</sub></sub>, that holds for a range of 3 orders of magnitude in SFR and for the last 11 billion years. As was the case for the Main sequence we discussed before, starbursts outliers do exist, exhibiting enhanced SFR for the available amount of gas, but they only consist of the  $\sim 10\%$  of star-forming population at each cosmic time (e.g. Sargent+14). Taking the ratio of the M<sub>H<sub>2</sub></sub> to the SFR one can define the gas depletion time, a parameter that quantifies in how much time a galaxy will run out of gas if it keeps forming stars and its current pace and if there is no external gas accretion. The fact that the majority of SFGs have a  $t_{\text{dep}}$  between 0.5-1 Gyrs over the last 12 Gyrs, can only

be explained if there is external in-fall of fresh gas from the intergalactic medium into the galaxies, to replenish the gas reservoir required and to sustain their star formation. This is one of the strongest evidence for the existence of *the holy grail of galaxy evolution* i.e. of cold gas accretion along the web filaments which is an irreplaceable feature in all hydrodynamical simulations, but which is yet to be directly observed (Dekel +09).

### A model of galaxy evolution and the missing pieces

The scaling relations between M\*-SFR-Mgas described above, along with other lines of evidence that touch upon the radiation field, the dust temperature, the morphology, the kinematic and the physical condition of the ISM, point towards an astonishing and unexpected homogeneity in the properties of galaxies that holds (at least) for the last 11 billion years. In the emerging paradigm (Fig.3) the vast majority of the star-forming galaxies up to  $z \sim 4$  (and maybe beyond) grow along the MS via a normal-steady mode of star-formation, before quenching mechanisms (that we still do not fully understand) shut their star formation down and drop below the main sequence (e.g. Magdis+21). On the other hand, a small fraction (about  $\sim 10\%$ ) of SFGs at any redshift, undergo a short, star-bursting event, possibly triggered by galaxy interactions, that elevates their SFR above the main sequence, increases their star formation effi-

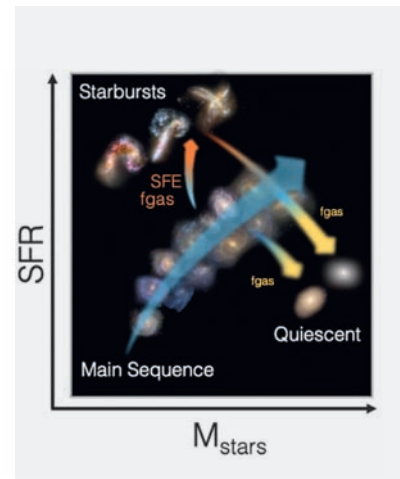


**Figure 3:** A schematic of the galaxy evolution paradigm based on the main sequence of star formation.

ciency by consume their available gas reservoir in short-time scales and they eventually die off moving in the region of quiescent/passive galaxies. All these processes are regulated by gas inflows (and outflows) within the galaxies and the dark matter haloes they reside.

While this framework is currently considered a benchmark in the studies of galaxy evolution and a basis for contemporary theoretical models, it can be regarded as a starting point for understanding galaxy evolution as there are still many critical pieces that are missing. First of all, there is still very little that we know about our cosmic morning with only scarce detections of galaxies within the first 0.5 Gyrs after the Big Bang. It is that imperative that we push the redshift frontier into  $z > 10$ , to identify the first galaxies, the first black holes, the first metals and the census of star formation in the early universe. Secondly, we need a better understanding of the physics and the internal processes that dictate the baryonic cycle within galaxies. For example, one of the major conundrums is why galaxies die and more importantly what keeps them dead. Finally, we need a multi-scale approach from the central core of the galaxies to the outskirts of their dark matter haloes and the large-scale structure in order to establish the halo-galaxy connection, to get direct detection of the elusive gas inflows that keep the galaxies running and explore the clusters as sites of accelerated evolution. To put it simply, we require a quantum leap in look back time, in detail and in scale.

We are now entering a period where all these three requirements are (or will soon be) met thanks to an impressive array of the most ambitious and technologically advanced space and ground based astronomical facilities and instruments that are progressively becoming available and are specifically built to address these questions. Among others some example of these flagship facilities include the Euclid Space telescope to be launched by ESA in the summer of 2023 aiming to chart the geometry of the Universe and identify the most massive structures of our cosmos, the Extremely Large Telescope (ELT) which is 39.3m telescope built by ESO that will see first light in 2028 and the Square Kilometer Array (SKA), built in Australia and South Africa that will trace the 21cm line mapping a billion galaxies out to the edge of the observable Universe and penetrate through the epoch re-ionisation providing observational data from the dark ages of Universe. However, and quite naturally, at the moment the interest of the astronomical community is focused on the largest, most powerful (and most expensive) space telescope ever build, the JWST.

## Galaxy evolution in the era of JWST

Following an impeccable launch on the Christmas day of 2021, and after a six-month commissioning period during its journey to the L2 point, JWST's performance and data quality have exceeded any expectation. While the community is still trying to familiarise with the capabilities of the telescope and the unprecedented images and spectra it delivers, the first science results indicate that we will soon need to revisit the galaxy evolution chapters of our textbooks. Below I briefly touch upon a far from exhaustive list of "first-light" results that have caught considerable attention in these early days of galaxy evolution studies with JWST.

### Breaking records

Until the summer of 2022, the record of most distant galaxy with a confirmed spectroscopic redshift was at  $z \sim 10$  (i.e. about 13Gyrs lookback time) with another dozen or so having secured redshifts at  $8 < z < 10$ . Since then, and with the delivery of the JWST data from the early release and GTO programs, the demographics of the detected galaxies

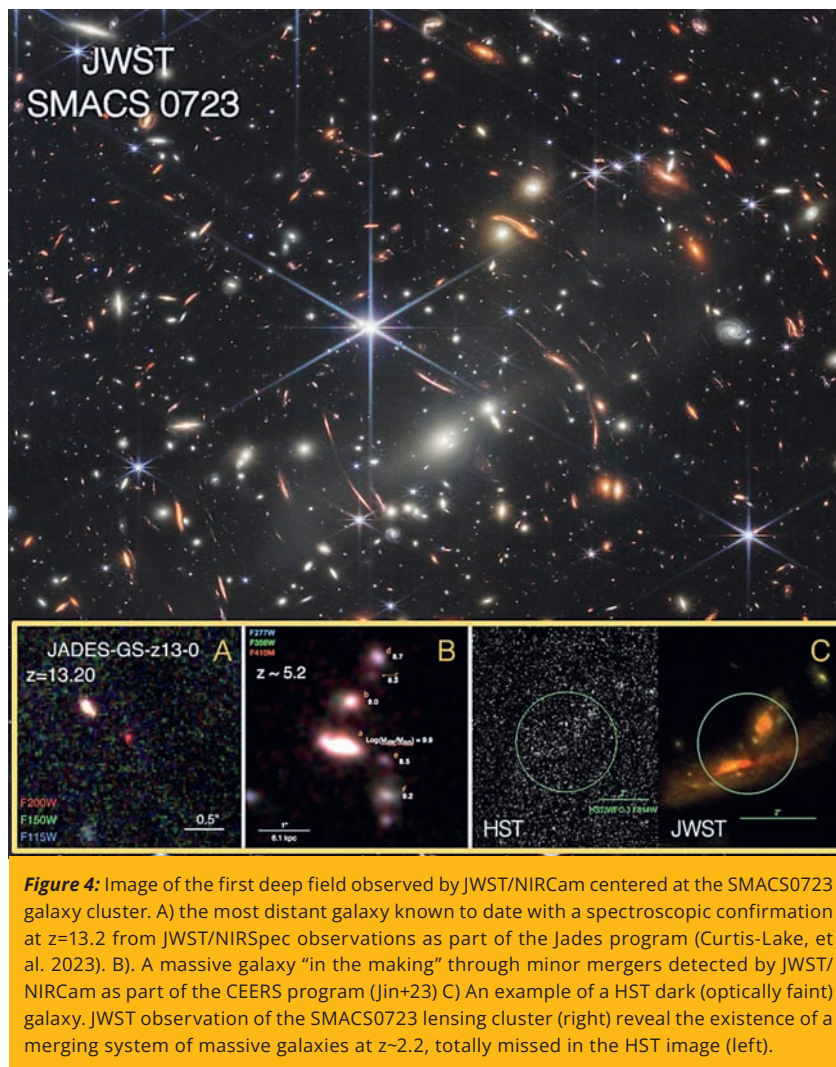


**Figure 4:** Image of the first deep field observed by JWST/NIRCam centered at the SMACS0723 galaxy cluster. A) the most distant galaxy known to date with a spectroscopic confirmation at  $z=13.2$  from JWST/NIRSpec observations as part of the Jades program (Curtis-Lake, et al. 2023). B). A massive galaxy “in the making” through minor mergers detected by JWST/NIRCam as part of the CEERS program (Jin+23) C) An example of a HST dark (optically faint) galaxy. JWST observation of the SMACS0723 lensing cluster (right) reveal the existence of a merging system of massive galaxies at  $z \sim 2.2$ , totally missed in the HST image (left).

in the epoch of re-ionisation has been increasing on a weekly basis with the one breaking record coming after the other (e.g. Filkenstein+22). At the moment this review is written, the most distant galaxy identified so far is at  $z=13.2$  (400Myrs after the Big Bang) in the GOODS-S field that was observed as part of JADES GTO program (Fig.4A, Curtis-Lake+23). Using JWST/NIRCam to photometrically identify high- $z$  galaxies and JWST/NIRSpec for a spectroscopic follow-up, candidate sources at redshifts as high as  $z \sim 16$  are awaiting spectroscopic confirmation, capturing an epoch in the history of the universe that was never observed before<sup>1</sup>. At the same time the unprecedented resistivity of JWST is also capable of detecting low mass galaxies ( $M_{\text{star}} < 10^9 M_{\odot}$ ) at  $z > 4$  and thus the satellites within the halo

1. A few hours after this sentence was written, preliminary analysis of incoming NIRSpec data indicate that the  $z \sim 16$  candidate turns out to be at  $z \sim 5$ .

of more massive galaxies at these redshifts. This opens the window for the exploration of “proto-massive” galaxies and the role of minor mergers as the avenue of the growth of galaxies during the period leading to the cosmic noon (Fig.4B Jin+23).

### Too many, too massive too early

Another puzzling result that emerged from the early release JWST imaging data is the existence of numerous, candidate, massive galaxies with in the first 600Myrs after the Big Bang. If the inferred stellar masses ( $M_{\text{star}} > 10^{10-11} M_{\odot}$ ) and redshifts ( $7.4 \leq z \leq 9.1$ ) are spectroscopically confirmed and fiducial masses are correct, then the mass density in the most massive galaxies would exceed the total previously estimated mass density (integrated down to  $M_{\text{star}} = 10^8 M_{\odot}$ ) by a factor of  $\sim 2$  at  $z \sim 8$  and by a factor of  $\sim 5$  at  $z \sim 9$  (Labbe+23). A more fundamental issue is that these stellar mass densities are difficult to realize in a standard LCDM

cosmology as the fiducial mass densities push against the limit set by the number of available baryons in the most massive dark matter halos. Of course, these results need to be scrutinized to dismiss alternative, and probably more likely explanations (e.g. erroneous redshifts or overestimated stellar masses due to the presence of an AGN or a top-heavy IMF) before we declare a crisis in our standard cosmological model.

### The population of “shy giants”

Recent ALMA observations revealed a population of fully-grown galaxies at  $4 < z < 6$  with a colossal amount of dust and gas that has kept them invisible so far from our optical surveys (e.g. Jin+19,22 Wang+19, Manning+22). The discovery of these “shy” giants showcased that pre-JWST cosmological surveys have not only missed the small and faint galaxies in the early Universe, but also big, fully-grown galaxies that have formed billions of stars within the first

20% of cosmic history. Near and mid-IR imaging with JWST/NIRCam and JWST/MIRI is now detecting the census of these HST-dark (or optically dark) sources, as they have been coined, and will determine their contribution in the total SFRD and stellar mass density budget in the Universe (Fig.4C, e.g. Kokorev+23). At the same time JWST/NIRSpec and JWST/MIRI spectroscopy along with ALMA follow-up observations aim to fully characterise their ISM and guide current hydro-dynamical models that fail to reproduce these systems in the early Universe.

### Dead galaxies in the early Universe

Perhaps one of the biggest unsolved questions in galaxy formation is the “quenching” of star formation and the mechanisms that keep galaxies “red and dead” over a large fraction of cosmic time. Recent observations have shown

that dead galaxies emerge at least as soon as  $z = 4$ , posing challenges to current theoretical models that struggle to accommodate their existence at these early times (e.g. Valentino+20). Furthermore, the physical mechanisms that led to the termination of star formation in these galaxies remain largely unconstrained. JWST imaging and spectroscopic follow up observations have already identified quiescent systems at lower stellar masses ( $M_{\text{star}} < 10^{10} M_{\text{sun}}$ ) and higher redshifts, deep into the epoch of re-ionisation. The emerging number density of quenched systems in the early universe ( $n \sim 1-2 \times 10^{-5} \text{ Mpc}^{-3}$ ) is two orders of magnitude higher compared to the theoretical predictions revealing a gap in our standard galaxy formation scenarios (e.g. Valentino+23, Carnall+23).

The golden era of galaxy evolution has just began.



## References

- Carnall, A., et al. 2023, MNRAS, 520, 3974  
Curtis-Lake, E., et al. 2023 arXiv221204558 (submitted to Nature)  
Dekel, A., et al. 2009, Natur, 457, 451  
Elbaz, D., et al. 2007, A&A, 468, 33  
Elbaz, D., et al. 2011A&A, 533, 119  
Finkelstein, s., et al. 2022, ApJ, 940, 55  
Genzel, R., et al. 2015, ApJ, 800, 20  
Jin, S., et al., 2019, ApJ, 887, 144  
Jin, S., et al., 2022, A&A, 665, 3  
Jin, S., et al., 2023, A&A, 670, 11  
Kokorev, V., et al., 2021, ApJ, 921, 40  
Kokorev, V., et al, 2023, ApJ, 945, 25  
Labbe, I., et al. 2022arXiv220712446 (accepted in Nature))  
Madau, P., & Dickinson, M., 2014, ARA&A, 52, 415  
Magdis, G.E, et al. 2010, MNRAS, 401 1521  
Magdis, G. E., et al. 2012, ApJ, 760, 6  
Magdis, G.E., et al. 2012, ApJ, 758, 9  
Magdis, G.E., et al. 2017, A&A 603, 93  
Magdis, G.E., et al. 2021, A&A, 647, 33  
Manning, S., et al. 2022, ApJ, 925, 23  
Noeske, K. G., et al. 2007ApJ, 660, 43  
Schreiber, C., et al. 2015, A&A, 575, 74  
Tacconi, L., et al. 2018, 853, 179  
Valentino, F., et al. 2018, ApJ, 869, 27  
Valentino, F., et al. 2020, ApJ, 889, 93  
Valentino, F., et al. 2023, arXiv230210936 (accepted in ApJ)  
Wang, T., et al. 2019, Natur, 572, 211

# Geomagnetically Induced Currents: a potential threat to our technological world

by Adamantia Zoe Boutsis<sup>1,2</sup> and George Balasis<sup>1</sup>

<sup>1</sup>Institute for Astronomy, Astrophysics, Space Applications and Remote Sensing (IAASARS), National Observatory of Athens (NOA), Athens, Greece

<sup>2</sup>Department of Physics, National and Kapodistrian University of Athens (NKUA), Athens, Greece

## What are GICs and why are we interested in them?

**S**olar Wind (SW) is a strong flux of plasma which is essentially protons and electrons coming from the Solar Corona. SW propagates in every direction from the Sun (radially) at a speed of about 400 km/s. The SW speed, density, temperature and composition are not uniform, but change as a function of the solar latitude. SW changes the shape of the geomagnetic field, as it approaches the Earth's magnetosphere. The magnetic field lines facing the Sun (dayside) become compressed while the nightside magnetic field lines are stretched. The plasma carried by the SW is forced to flow around the magnetosphere (plasma is "frozen in" the magnetic field). The SW would burn our atmosphere in absence of the magnetic field, but we are shielded. Thanks to the Earth's magnetic field the SW cannot flow inside the magnetosphere and is deflected. Yet, there are particular case events where the SW plasma can reach the Earth's atmosphere – **magnetic storms**.

During times of heightened space weather, intense solar flares and associated plasma clouds are expelled from the Sun. Known as Coronal Mass Ejections (CMEs), these magnetic clouds can sometimes head directly towards the Earth hitting the Earth's magnetosphere around 1-3 days later. This will result in a magnetic storm.

Systems on or near Earth such as Global Positioning System (GPS) and electricity networks are increasingly vulnerable to damage by intense space weather events (such as magnetic storms) and human activities are increasingly dependent on such systems (<https://geomag.bgs.ac.uk/education/gic.html>). Space weather affects various techno-

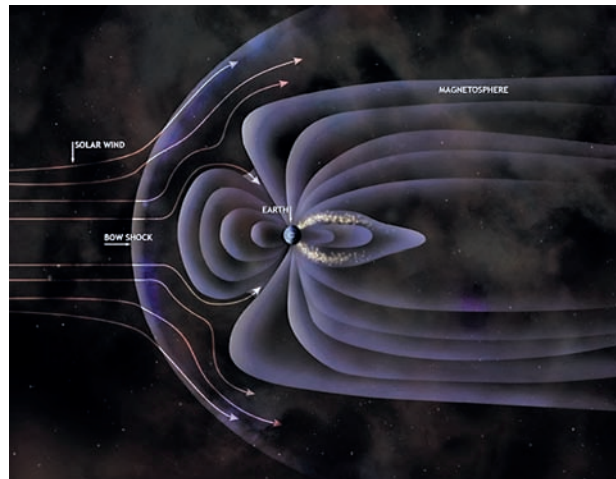


**Figure 1:** Schematic Illustration of the Earth's magnetosphere. Credits: <https://www.jpl.nasa.gov/infographics/earths-magnetosphere>.

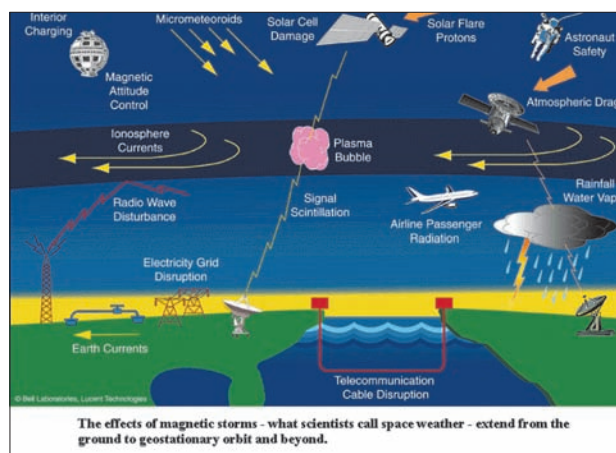


**Figure 2:** The effects of magnetic storms extend from the ground to geostationary orbit and beyond. Copyright: Bell Laboratories, Lucent Technologies.

logical systems on Earth, such as:

- Corrosion of pipelines
- GPS scintillation
- Effects on telecommunications
- Radiation for civil flights over poles
- Disruption of national power grids
- Perturbation on radio-waves
- Satellites malfunction

The most serious effects on human activity occur during major magnetic storms, induced by CMEs. During a magnetic storm, the principal magnetospheric currents and the connected ionospheric currents are intensified caus-

ing rapid changes in the geomagnetic field. These variations generate Geomagnetically Induced Currents (GICs) at ground that can disrupt the operation of power grids, magnetic surveying, etc. GICs, often referred to as the ground end of the "space weather" chain: Sun – solar wind – magnetosphere – ionosphere – Earth's surface, can have cumulative and long-term effects on transformers and many failures, attributed to "ageing" and "manufacturing defects," could actually be the result of the stress accumulated over the years caused by GICs flowing.

Some well-known historical GIC events are:

1. The phenomenon of geomagnetic currents was first noticed in 1847. In this year, the telegraph was the primary method of communication and relied on batteries for power. Once, however, while an Aurora Borealis was occurring, telegraph operators observed a disruption in the transmission of communications. When the power was switched off, the GICs 1 or “celestial power” allowed transmissions to be conducted at a better quality than with the use of batteries (<https://www.solarstorms.org/CanadaPipelines.html>).
2. September 1859 (Carrington Event): Telegraph systems all over Europe and North America failed, in some cases giving telegraph operators electric shocks. Telegraph pylons threw sparks.
3. March 1989 Storm: Collapse of the power grid in North-East Canada (9-hour outage of Hydro-Québec’s electricity transmission system)
4. Halloween 2003 Storms – Power outage in Sweden for about an hour. Some transformer failures were reported in South Africa! They were associated with long-lasting (low intensity) GIC exposure.

A recent USA Government research on the economic impact of the occurrence of another “once in a century” severe magnetic storm (such as the 1859 “super storm”), shows potential costs on the Nation’s power grid of \$1-2 trillion ([https://obamawhitehouse.archives.gov/sites/default/files/microsites/ostp/space-weather\\_2013\\_report.pdf](https://obamawhitehouse.archives.gov/sites/default/files/microsites/ostp/space-weather_2013_report.pdf)).

### The physics behind GICs

The physics behind GICs is related to the Faraday’s law of induction:

$$\vec{\nabla} \times \vec{E} = -\frac{\partial \vec{B}}{\partial t}$$

where  $\vec{E}$  is the geoelectric field and  $\vec{B}$  is the geomagnetic field. The equation above relates the temporal variation of the geomagnetic field to the formation of the geoelectric field that drives GICs at the ground according to Ohm’s law  $\vec{j} = \sigma \vec{E}$ , where  $\vec{j}$  is the current density at a given location and  $\sigma$  is a material-dependent parameter called the conductivity.

It is important to highlight that  $\vec{E}$  depends only on the magnetospheric-ionospheric current system and on the Earth’s geology (Pirjola, 1982). Since  $\vec{j}$  is difficult to evaluate ( $\sigma$  is a tensor), typically the current (GIC) flowing through a particular network is evaluated (Piersanti and Carter, 2020 and reference therein). Following the approach of Pirjola (2000, 2002), the GIC calculation consists of two steps:

1. estimation of the geoelectric field through the evaluation of the magnetospheric and ionospheric currents, and the knowledge of the conductivity at ground (geophysical step);
2. calculation of the flowing GIC through the determined geoelectric field and the knowledge of the particular power network (engineering step).

Since the geoelectric field is the primary driver of GICs, it is, therefore, the principal quantity that determines their magnitude. Once  $E$  is known, it is relatively easy to take the second step for the evaluation of the GIC flowing through a power network (Pirjola, 2000). In fact, assuming the geoelectric field as spatially constant, the GIC can be calculated as:

$$GIC = aE_x + bE_y$$

where  $a$  and  $b$  are the network-specific coefficients at each network node depending only on the resistance and geometrical composition of the system (Viljanen and Pirjola, 1994),  $E_x$  and  $E_y$  components indicate the North and East directions of the  $E$  field, respectively, and GIC is the current in [A].

Typically,  $a$  and  $b$  vary in the range of 0–200 A km/V (Pulkkinen et al., 2012). GIC enter a power grid through earthed transformer neutrals (“earthing currents”) and flow along transmission lines (“line currents”) to other transformers, at which they go back to the ground. A GIC path between two transformers is shown in Figure 3.

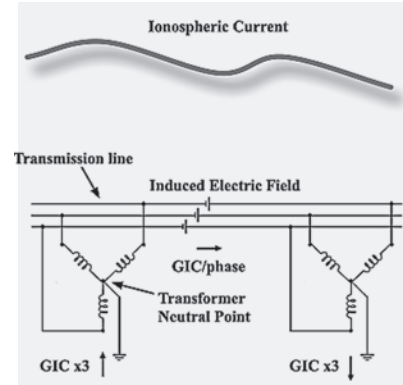


**Figure 3:** (Figure 1 from [Wik et al., 2008]) Geomagnetically induced currents (GIC) flowing along the transmission line between two transformers. A time-varying ionospheric current, i.e., the primary driver of GIC, is also schematically shown.

### The Hellenic GeoMagnetic Array (ENIGMA)

The National Observatory of Athens (NOA) operates the Hellenic GeoMagnetic Array (ENIGMA), a network of 4 ground-based magnetometer stations in the areas of Klokotos (abbreviated as THL), Dionysos (DIO), Velies (VLI), and Finokalia (FIN), located in central and southern Greece (<http://enigma.space.noa.gr/>). ENIGMA monitors the geomagnetic field variations associated with the

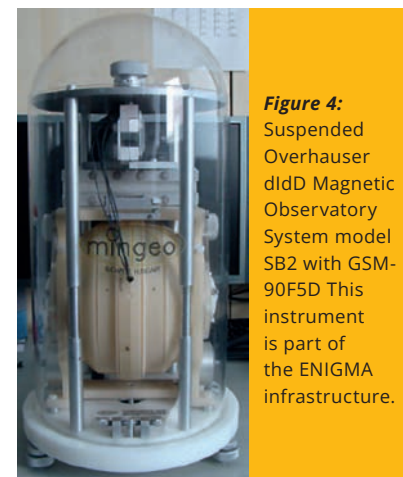


**Figure 4:** Suspended Overhauser dIdD Magnetic Observatory System model SB2 with GSM-90F5D This instrument is part of the ENIGMA infrastructure.



**Figure 5:** D/I theodolite THEO 010. This instrument is part of the ENIGMA infrastructure.

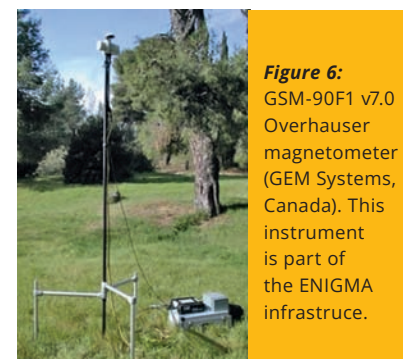


**Figure 6:** GSM-90F1 v7.0 Overhauser magnetometer (GEM Systems, Canada). This instrument is part of the ENIGMA infrastructure.

occurrence of magnetic storms and ultra low frequency (ULF) waves using vector fluxgate magnetometer instruments. ENIGMA is a SuperMAG (<http://supermag.jhuapl.edu/>) contributor, a worldwide collaboration of organizations and national agencies that currently operate more than 300 ground-based magnetometers (Gjerloev, 2009). Figures 4-6 show part of IAASARS/NOA ground-based magnetometry infrastructure.

## A study of GIC in the Mediterranean region

Traditionally, it was thought that only electricity networks located in high latitudes (Northern America, Scandinavia) are affected by GIC (the Auroral Electrojet system plays an important role on the polar regions), but similar effects can be observed in lower latitudes, as well. This is confirmed by the recently reported existence of electrical power problems in areas of low latitudes (Spain, S. Africa, Japan, China), that is latitudes similar to those of Greece (e.g. (Torta et al., 2014) and (Koen & Gaunt, 2003)).

GIC flowing at low and middle latitudes are linked to ionospheric source fields different from the ones observed at high-latitudes (e.g., auroral electrojets, which are horizontal electric currents that flow in the ionosphere of the auroral zone). According to Kappenman (2005) the source of sustained GIC at low and middle latitudes is linked to high rates of change (of the geomagnetic field) associated with impulsive increases in the solar wind's dynamical pressure or ring current intensification. In these regions, maximum values of the time variation of the magnetic field's horizontal component ( $dB_H/dt$ ) usually occur at the abrupt storm onset and not during its main phase, therefore vulnerability is higher around these times (Kappenman, 2003). The GIC index was initially introduced by Marshall et al. (2010). It is derived entirely from geomagnetic field data, without need of knowing the ground conductivity, ionospheric current system geometry and the relevant infrastructure details and, therefore, acts as a geoelectric field proxy. It has two components; GIC<sub>x</sub> index derived from the East (Y) component of the geomagnetic field and GIC<sub>y</sub> index derived from the North (X) component. According to the authors, the superiority of the GIC index over  $dB_H/dt$  is due to the frequency dependence between the geoelectric field and  $dB_H/dt$  as discussed by

Pirjola (1982). The index has been tested in various studies (e.g., Tozzi, Coco, et al., 2019; Tozzi, De Michellis, et al., 2019) and seems to perform well for low and middle latitudes, which is to say it tracks the historical instances of increased GIC risk with minimal input requirements.

While such an index does not, and cannot, on its own provide information on the geoelectric field (lacking any input on ground conductivity) or the actual effect on technological infrastructure (lacking any input on the topology or load of an affected network), it has the advantage of being a consistent measure that can be combined with ground conductivity models of one's choice and juxtaposed on any current or future infrastructure one is interested in. For a single location, the GIC index is a good measure of relative risk over time, under the reasonable assumption that the GIC flow at a node in the pipeline or power transmission network is proportional to the local geoelectric field. Comparison across locations that may have different geology is then less of a measure of the possible impact (due to variations in conductivity) and more of a measure of the "geoeffectiveness" of the driving magnetic field fluctuations (e.g., Pulkkinen et al., 2015) that can be used to illustrate the likely response for different conductivity regions.

In a recent study Boutsis et al. (2023) presented the results of a preliminary analysis on the geophysical conditions known to generate GIC, by calculating

the GIC index, a useful GIC proxy for high-level studies, in four different locations which host ENIGMA, complemented by data analysis of magnetic observatories in the Mediterranean region. They focused on the four most intense magnetic storms of solar cycle 24 (Disturbance storm time index (Dst) < -150 nT) to make an assessment of the GIC-imposed risk in Greece and the wider Mediterranean region. For estimates of the geoelectric field at each location, one dimensional (1-D) layer models can be employed; with compilations of such models for larger areas (e.g., Kelbert, 2019). For Europe, one such compilation is provided by the EURISGIC project (Ádám et al., 2012; Viljanen et al., 2012, 2013) and it has been used to put the GIC proxy values in context.

In order to extend this study toward the wider Mediterranean region, they employed data from six magnetic observatories located in Italy (Castello Tesino - CTS), France (Chambon la Forêt - CLF), Spain (Ebro - EBR and San Fernando - SFS), Algeria (Tamanrasset - TAM) and Turkey (Izник - IZN). Although not all observatories are ideally located close to the Mediterranean, they were selected as the best available options in terms of location and data availability (e.g., TAM is relatively remote, but the best available observatory in the southern expanse). A map of all the geomagnetic stations/observatories used for this study, in geographic coordinates is shown in Figure 7.

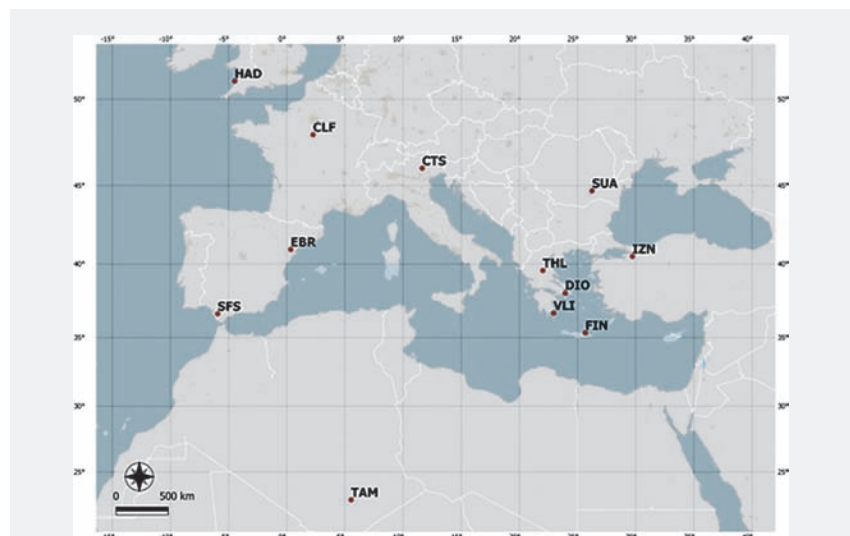


**Figure 7:** (Figure 1 from [Boutsis et al., 2023]) Geographic map displaying all the geomagnetic stations/observatories used for the present study. From North to South: Hartland (HAD, United Kingdom), Chambon la Forêt (CLF, France), Castello Tesino (CTS, Italy), Surlari (SUA, Romania), Ebro (EBR, Spain), Iznik (IZN, Turkey), Klokotos (THL, Greece), Dionysos (DIO, Greece), Velies (VLI, Greece), San Fernando (SFS, Spain), Finokalia (FIN, Greece), and Tamanrasset (TAM, Algeria).

Selected case studies focus on the strongest geospace magnetic storms of solar cycle 24. Based on Dst index values (<http://wdc.kugi.kyoto-u.ac.jp/dstdir/index.html>) less than  $-150$  nT, the events under investigation occurred

on 17 March 2015, 23 June 2015, 20 December 2015, and 26 August 2018. During the aforementioned events the Dst index reached the minimum values of  $-223$ ,  $-204$ ,  $-155$ , and  $-174$  nT, respectively (Table 1).

**Table 1:** (Table 1 from [Boutsi et al., 2023]) Strongest Geospace Magnetic Storms of Solar Cycle 24 (2008–2019), Based on Minimum Dst Index Values. SC stands for Sudden Commencement.

Case	SC date	SC time (UT)	Storm date	Storm time (UT)	Dst (nT)
#1	17/03/2015	04:45:00	17/03/2015	22:00:00	-223
#2	21/06/2015	16:44:00	–	–	–
	22/06/2015	05:44:24	23/06/2015	04:00:00	-204
#3	22/06/2015	18:33:00	–	–	–
	19/12/2015	16:16:12	20/12/2015	22:00:00	-155
#4	N/A	N/A	26/08/2018	06:00:00	-174

Figure 8 focuses on the 2015 St. Patrick's Day magnetic storm, displaying results from CTS, DIO and VLI. In each panel the Dst index is represented in cyan, magnetic field data in gray and the GIC index in blue. Additionally, green and yellow dashed lines represent the risk level thresholds (Marshall et al., 2011; Tozzi, De Michelis, et al., 2019). X-axis covers a time period of 3 days, right Y-axis corresponds to the geomagnetic field data (and Dst index) and left Y-axis corresponds to the GIC index. The three panels on the left depict Bx and the GICy index, respectively, while the three panels on the right depict By and the GICx index. In all panels a red arrow pointing on the X-axis denotes the Storm Sudden Commencement (SSC). During the 2015 St. Patrick's Day magnetic storm, the strongest magnetic

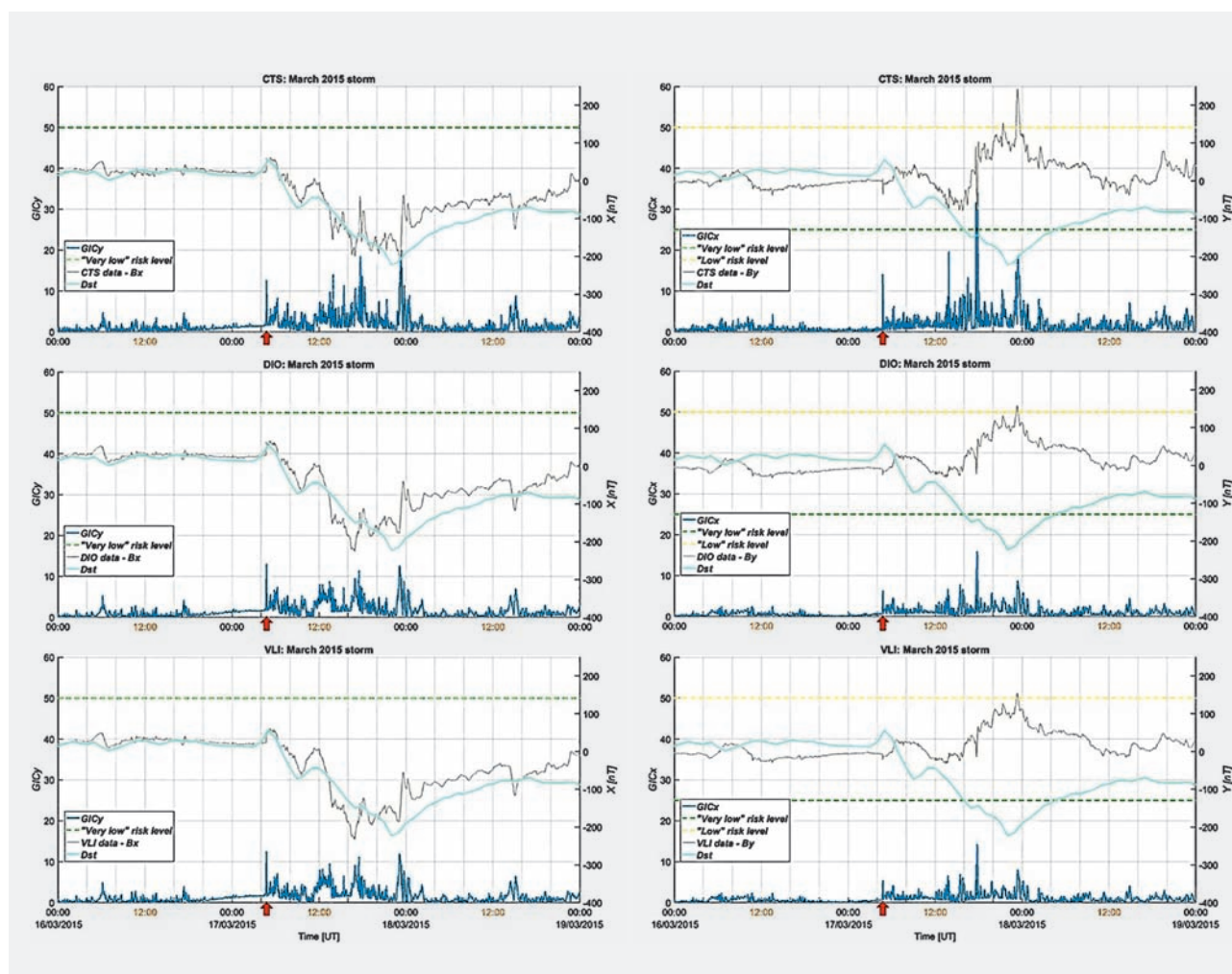


**Figure 8:** (Figure 2 from [Boutsi et al., 2023]) Storm of 17 March 2015: (From top to bottom the magnetic stations/observatories are: CTS, DIO and VLI). In each panel are shown the Dst index (in cyan), the geomagnetic field's X (left column) or Y component (right column) (in gray, right y-axis) and the GICy (left column) or GICx index (right column) (in blue, left y-axis). Green and yellow dashed lines represent the risk levels, associated with the geomagnetically induced current index values, according to Marshall et al. (2011). The arrow pointing on the x-axis denotes the sudden commencement of the storm, according to International Service of Geomagnetic Indices.

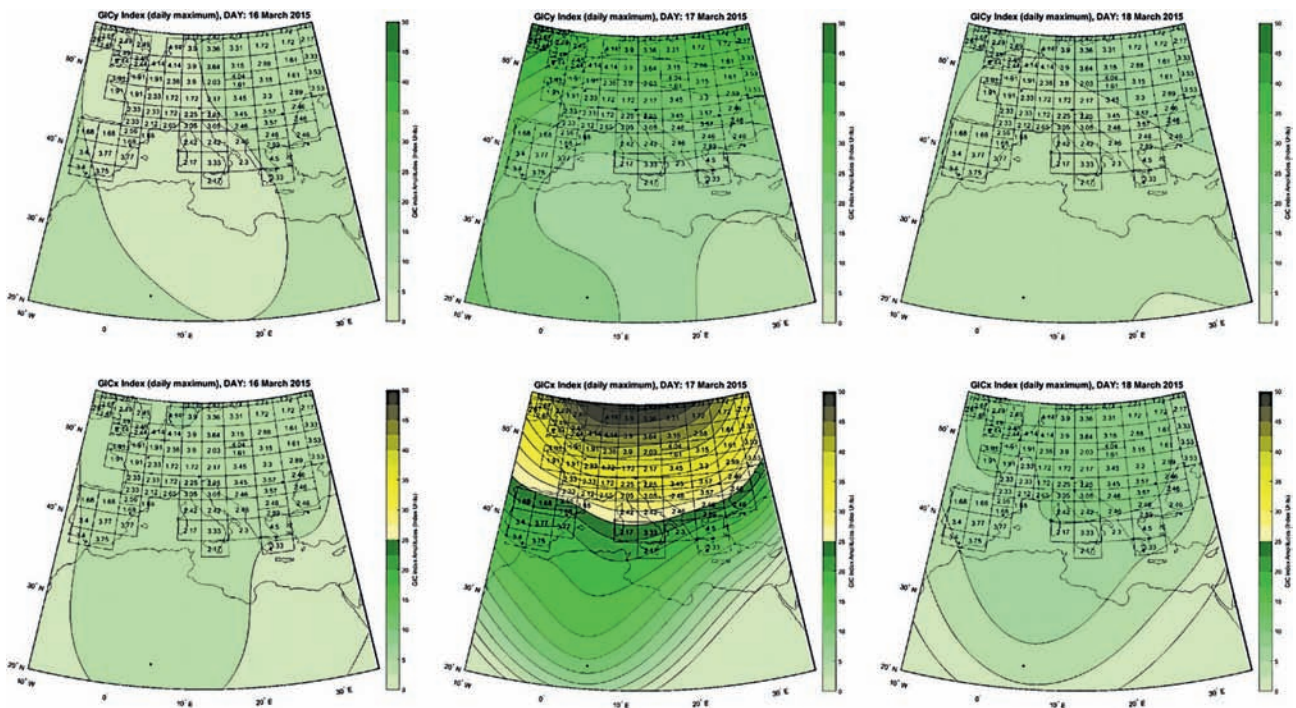


**Figure 9:** (Figure 7 from [Boutsi et al., 2023]) Contour maps of GICy (top panels) and GICx (bottom panels) indices for 16, 17, and 18 March 2015. Here, we zoom in the “Very Low” (available for GICy and GICx) and “Low” (available for GICx) risk levels, represented by green and yellow colors, and thus different intensities of geomagnetically induced current index can be identified by the different hues of green/yellow. Focus is on geographic latitudes between 20° and 55° and geographic longitudes between -10° and 35°. Red dots represent locations of magnetic stations/observatories. Overplotted is a ground conductivity map of Europe in the form of a grid, each cell of which corresponds to a 1-D ground model (Ádám et al., 2012), denoted by its respective conductances (in base 10 logarithmic scale, with units of log(S)) with an integration depth of 80 km.

storm of solar cycle 24, maximum GICy index values for DIO, VLI and TAM stations occur around the SSC, while maximum GICx index values for all stations/observatories occur after the SSC and during the storm’s main phase (i.e., around 4 hr before the minimum Dst, for the majority of the stations). Still, in all stations/observatories they observed a local increase of both the GICy and the GICx index around the SSC. Another observation is that the GICy index values obtained around the SSC seem to increase as one moves toward lower latitudes for the majority of the stations/observatories, while the GICx index values seem to decrease.

Furthermore, an attempt to produce GIC index maps for the Mediterranean region, focusing on the 2015 St. Patrick’s Day storm was made. Based on the GIC risk level scale of Marshall et al. (2011) and on daily maximum GIC index values they derived contour maps (using biharmonic spline interpolation) in geographic latitude versus geographic longitude of GIC index values for 3 days, zooming in what happens within the low-

est activity levels (“very low” and “low”) (Figure 9). In order to prevent edge effects embedded in the contouring algorithm, they had to employ auxiliary geomagnetic data from two magnetic observatories outside the Mediterranean region, namely Hartland (HAD) in the United Kingdom and Surlari (SUA) in Romania. The GIC index maps can be considered as a preliminary modeling attempt of GIC activity levels in the Mediterranean region.

For a better assessment of the geoelectric field that may be associated with these GIC indices they overplotted a ground conductivity map of Europe in the form of a grid, each cell of which corresponds to a 1-D ground model by Ádám et al. (2012) as denoted by its respective number. The parameters for each model (resistivity and thickness for each layer) are openly available at <http://real.mtak.hu/2957/>. In short, each cell is divided into several layers, of varying depths, with corresponding resistivities. Its conductance up to a certain depth is then calculated by adding up all the intervening layer depths divided by

their resistivities. In Figure 7 instead of cell numbers are shown conductances for the upper 80 km.

Both the GICy and GICx indices have sparse contour lines before and after the storm, which doesn’t give much information on their structure; on the day of the storm occurrence contour lines of both indices tend to become tightly clustered, which shows a strong horizontal ordering with gradually increasing values from South to North. In other words, they observe a behavior similar to the one described for other intense magnetic storms (Balasis et al., 2006, 2008), as well as for the St. Patrick’s Day storm (Papadimitriou et al., 2020) where the transition from quiet-time to storm-time magnetosphere correlates with the transition from a state of higher complexity/lower degree of organization to a state of lower complexity/higher degree of organization for the complex system of the Earth’s magnetosphere.

In a nutshell:

1. GIC index values are elevated during the selected storms, although they do not exceed thresholds indicating

high risk for infrastructure installed at these locations.

2. GIC index increases appear simultaneously with the SSC occurrence, in agreement with other GIC studies for low and middle latitudes (e.g., Kappenman, 2003; Zhang et al., 2015).
3. Correlation coefficients between calculated electric fields and GIC indices range from 0.54 to 0.65 for the St. Patrick's Day storm.
4. The large disparity of ground conductivity values of 1-D layer ground models for Europe results in the expected electric fields varying by

a factor of over 100 even on the scale of countries such as Spain or Greece. This is in addition to variations by a factor of 2 in the calculated GIC index for those two countries during the height of St. Patrick's Day storm. This shows the inadequacy of using a single observatory for a nationwide index.

The derivation of the GIC index contour maps for the Mediterranean region, although based on a simple technique, gave an overall display of the GIC intensity distribution around the Mediterranean region for a magnetic storm. Fu-

ture work could involve more case studies as well as an evaluation of these preliminary results. Enhanced magnetopause currents due to large changes in the solar wind's dynamic pressure may pose threats to low and middle latitude power networks, of at least equal significance to those occurring during the main phase of large magnetic storms. Future work could focus on the impacts of sudden impulse (SI) events on power systems, which depending on latitude, might differ from that observed during large main phase storms.

## References

- Ádám, A., et al. 2012, Acta Geodaetica et Geophysica Hungarica, 47, 377
- Balasis, G., et al. 2006, Annales Geophysicae, 24, 3557
- Balasis, G., et al. 2008, Geophysical Research Letters, 35, L14102
- Boutsi, A. Z., et al. 2023, Space Weather, 21, e2022SW003122
- Kappenman, J. G. 2003, Space Weather, 1, 1016
- Kappenman, J. G. 2005, Space Weather, 3, S08C01
- Kelbert, A. 2019, Surveys in Geophysics, 41, 115
- Koen, J., & Gaunt, T. 2003, In 2003 IEEE Bologna power tech conference proceedings (Vol. 1)
- Marshall, R. A., et al. 2010, Space Weather, 8, S05002
- Marshall, R. A., et al. 2011, Space Weather, 9, S10004
- Papadimitriou, C., et al. 2020, Entropy, 22, 574
- Pirjola, R. 1982, Geophysica, 18, 1
- Pirjola, R. 2000, IEEE Transactions on Plasma Science, 28, 1867
- Pirjola, R. 2002, Surveys in Geophysics, 23, 71
- Piersanti, M. and Carter, B. 2020, Chapter 10 - Geomagnetically induced currents, Editor(s): Materassi, M., Forte, B., Coster, A. J., and Skone, S. The Dynamical Ionosphere, Elsevier, 121
- Pulkkinen, A., et al. 2012, Space Weather, 10, S04003
- Pulkkinen, A., et al. 2015, Earth Planets and Space, 67, 93
- Torta, J. M., et al. 2014, Earth Planets and Space, 66, 87
- Tozzi, R., Coco, I., et al. 2019, Annals of Geophysics, 62, 448
- Tozzi, R., De Michelis, P., et al. 2019, Space Weather, 17, 46
- Viljanen, A., & Pirjola, R. 1994, Surveys in Geophysics, 15, 383
- Viljanen, A., et al. 2012, Journal of Space Weather and Space Climate, 2, A17
- Viljanen, A., et al. 2013, Space Weather, 11, 575
- Wik, M., et al. 2008, Space Weather, 6, S07005
- Zhang, J. J., et al. 2015, Space Weather, 13, 643



Visit our website

<http://www.helas.gr>

The above web server contains information, both in greek and english, about the Hellenic Astronomical Society (Hel.A.S.), the major organization of professional astronomers in Greece. The Society was established in 1993, it has more than 250 members, and it follows the usual structure of most modern scientific societies. The web pages provide information and pointers to astronomy related material, useful to both professional and amateur astronomers in Greece. It contains a directory of all members of the Society, as well as an archive of all material published by the Society, including electronic newsletters, past issues of "Hipparchos", and proceedings of Conferences of Hel.A.S. The server is currently hosted by the University of Thessaloniki.

# The 16th Hellenic Astronomical Conference

26-28 June 2023, Athens

The 16th Conference of Hel.A.S. will take place in Athens, from 26 to 28 June 2023. During the conference we will celebrate the 30 year anniversary of the Society.

## Conference Venue

The science sessions of the 16th Conference of Hel.A.S. will take place at the 128 seat Drakopoulos Amphitheater, as well as the 116 seat Argyriadis Amphitheater, both of which are located in the Historic Building of the University of Athens.

The welcome reception and opening session with the public outreach talk will take place on Monday June 26, 2023, at 12:00 noon, at the central Amphitheater of the adjacent building of the Academy of Athens.

## Organizing Committees

### Scientific Organizing Committee (SOC)

SOC Chair: Vassilis Charmandaris, President of Hel.A.S.

SOC Members: J. Antoniadis, V. Archontis, G. Balasis, K.N. Gourgouliatos, E. Koulouridis, L. Moustakas, G. Panopoulou, A. Papaioannou, M. Petropoulou, D. Rigopoulou, K. Tassis

### Conference Sessions

Session 1: "Heliophysics and the Solar System"

Convenors: G. Balasis, A. Papaioannou, V. Archontis

Session 2: "Extragalactic Astronomy and Astrophysics"

Convenors: E. Koulouridis, L. Moustakas, D. Rigopoulou

Session 3: "Cosmology and Relativistic Astrophysics"

Convenors: K.N. Gourgouliatos, M. Petropoulou

Session 4: "Stars, Planets and the Interstellar Medium"

Convenors: J. Antoniadis, G. Panopoulou, K. Tassis

### Local Organizing Committee (LOC)

LOC Chair: M. Petropoulou (NKUA)

LOC Members: D. Hatzidimitriou (NKUA), E. Koulouridis (NOA), S. Dimitrakoudis (U. Alberta/NKUA), A. Nathanail (Academy of Athens), G. Vasilopoulos (NKUA)

## Invited Plenary Speakers

Session 1: "Heliophysics and the Solar System"

Prof. Yannis Zouganelis, ESA (Spain)

"Unlocking the Secrets of the Sun: Early Discoveries and Future Prospects of the Solar Orbiter Mission"

Session 2: "Extragalactic Astronomy and Astrophysics"

Dr. h.c. Natascha M. Forster Schreiber, Max-Planck-Institut fuer extraterrestrische Physik (Germany)

"Star-forming Galaxies at Cosmic Noon and Beyond"

Session 3: "Cosmology and Relativistic Astrophysics"

Prof. Dr. Michael Kramer, MPIfR (Germany) - "J.H. Seiradakis" Plenary Lecture

"Radio pulsars as probes of fundamental physics - and more"

Session 4: "Stars, Planets and the Interstellar Medium"

Dr. Jacques Laskar, IMCCE, Observatoire de Paris (France)

"Chaos in the Solar System. Historical perspective and new results."

## Invited Speakers

Session 1: "Heliophysics and the Solar System"

A. Belehaki (NOA, Greece), M. K. Georgoulis (Academy of Athens, Greece), A. Nindos (Univ. of Ioannina, Greece), K. Tsiganos (NKUA, Greece)

Session 2: "Extragalactic Astronomy and Astrophysics"

I. Georgantopoulos (NOA, Greece), G. Rodighiero (Univ. of Padova, Italy)

Session 3: "Cosmology and Relativistic Astrophysics"

D. Antonopoulou (Univ. of Manchester, UK), B. Reville (MPIK Heidelberg, Germany)

Session 4: "Stars, Planets and the Interstellar Medium"

T. Fragos (Univ. of Geneva, Switzerland), T. Karalidi (Univ. of Central Florida, USA), A. Tritsis (EPFL, Switzerland)

## Best PhD thesis Prize - Emilios Harlaftis

Dr. Raphael Skalidis, Caltech (USA)

Title of talk: "Estimating of the magnetic field strength in the interstellar medium"

Location/Time: East Hall Academy of Athens - Monday June 26, 2023 at 12:45

## Public Outreach Talk (in Greek)

Speaker: Prof. Vasiliki Pavlidou, Dept. of Physics, Univ. of Crete (Greece)

Title of talk: "Το σύμπαν είναι κατανοητό!"

Time: Monday June 26, 2023 at 20:00

Location: Stavros Niarchos Foundation Cultural Center, Hall "The Lighthouse - Φάρος"

## Social Events

The following events will take place during the conference:

**Monday June 26, 2023 at 12:00**

Opening Ceremony of the Conference (in greek) at the East Hall of the Academy of Athens

Honoring the past presidents of the Society

2023 Best PhD Thesis Prize - Emilios Harlaftis

Welcome reception and Conference registration

**Monday June 26, 2023 at 20:00**

Public Outreach Talk by Prof. Vasiliki Pavlidou, at "The Lighthouse - Φάρος" of the Stavros Niarchos Foundation Cultural Center.

**Monday June 26, 2023 at 21:30**

Star Gazing Event with the support of Greek Amateur Astronomers at the "Southern Trails" of the Stavros Niarchos Foundation Cultural Center

**Tuesday June 27, 2023 at 20:00**

Conference Dinner at the Gardens of the historic site of the National Observatory of Athens in Thissio.

**Wednesday June 28, 2023 at 19:00**

Public Outreach Talk by Dr. Jacques Laskar (Obs. de Paris & Académie des Sciences, France) at the Eugenides Foundation. The talk, entitled "A la recherche d'un scénario cohérent pour l'évolution du système Terre-Lune", will be in French with parallel translation in Greek. The event is organized by the Institut Français de Grèce.



# THE X-RAY UNIVERSE 2023

13-16 June 2023  
Athens, Greece

## SOC

Aya Bamba, University of Tokyo, Japan  
Didier Barret, Institut de Recherche en Astrophysique et Planétologie, Toulouse, France  
Stefano Bianchi, Università degli Studi Roma Tre, Italy  
Andrea Comastri, INAF Osservatorio di Astrofisica e Scienza dello Spazio, Bologna, Italy  
Anne Decourchelle, Commissariat à l'énergie atomique Saclay, Gif sur Yvette, France  
Maria Díaz Trigo, European Southern Observatory, Garching, Germany  
Megan Donahue, Michigan State University, East Lansing, USA  
Chris Done, University of Durham, United Kingdom  
Christine Jones, Harvard-Smithsonian Center for Astrophysics, Cambridge, MA, USA  
Ioannis Georgantopoulos, National Observatory of Athens, Greece  
Richard Griffiths, University of Hawaii, Hilo, USA  
Jimmy Irwin, University of Alabama, Tuscaloosa, USA  
Jelle Kaastra, SRON Netherlands Institute for Space Research, Leiden & Leiden University, NL  
Stefanie Komossa, Max-Planck-Institut fuer Radioastronomie, Bonn, Germany  
Antonio Maggio, INAF Osservatorio Astronomico di Palermo, Italy  
Miguel Mas Hesse, Centro de Astrobiología, Villanueva de la Cañada, Spain  
Richard Mushotzky, University of Maryland, College Park, USA  
Paul Nandra, Max-Planck-Institut für extraterrestrische Physik, Garching, Germany  
Lida Oskinova, University of Potsdam, Germany  
Ioannis Papadakis, University of Crete, Heraklion, Greece  
Katja Poppenhaeger, Leibniz-Institut für Astrophysik Potsdam, Germany  
Gregor Rauw, Université de Liège, Belgium  
Nanda Rea, Institute of Space Sciences (CSIC-IEEC), Barcelona, Spain  
Kathy Romer, University of Sussex, Brighton, UK  
Maria Santos-Lleo, European Space Agency, Villanueva de la Cañada, Spain  
Craig Sarazin, University of Virginia, Charlottesville, USA  
Manami Sasaki, University of Erlangen-Nürnberg, Germany  
Norbert Schartel (co-chair), European Space Agency, Villanueva de la Cañada, Spain  
Jürgen Schmitt, Hamburger Sternwarte, Germany  
Martin Ward, University of Durham, United Kingdom  
Michael Watson, University of Leicester, United Kingdom  
Natalie Webb, Institut de Recherche en Astrophysique et Planétologie, Toulouse, France  
Rudy Wijnands (chair), University of Amsterdam, The Netherlands

## Topics:

Stars, White Dwarfs, & Solar System  
Exoplanets and their Host Stars  
White Dwarf Binaries, Neutron Star and  
Black Hole Binaries, & ULXs  
Supernovae, SNRs, Isolated Neutron Stars,  
& Diffuse Emission  
Galaxies & Galactic Surveys  
Active Galactic Nuclei  
Groups of Galaxies, Clusters of Galaxies,  
& Superclusters  
Cosmology & Extragalactic Deep Fields  
Current & Future Missions

## LOC

Thanassis Akylas  
Lucia Ballo  
Ignacio de la Calle  
Jacobo Ebrero  
Felix Fürst (chair)  
Ioannis Georgantopoulos  
Aitor Ibarra  
Elena Jiménez Bailon  
Celia Sánchez  
Richard Saxton  
Norbert Schartel  
Martin Stuhlinger  
Ivan Valtchanov



<http://xrayuniverse.esa.int>

# Back issues of Hipparchos

Hipparchos is the official newsletter of the Hellenic Astronomical Society. It is distributed by post to the members of the society. You can download back issues from: <http://www.helas.gr/news.php>

